Molecular Cell

Article

Polysome collapse and RNA condensation fluidize the cytoplasm

Graphical abstract

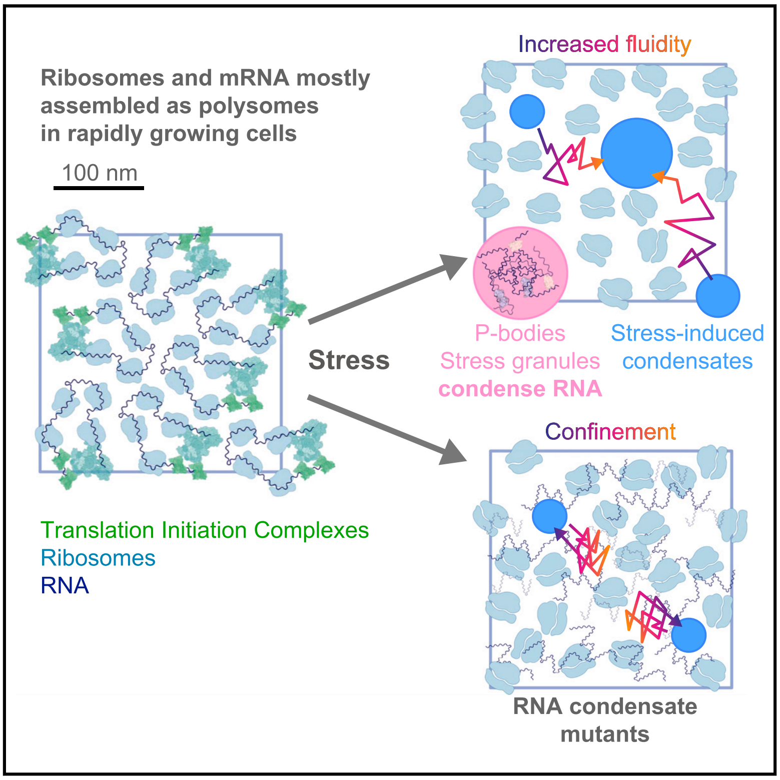

Highlights

- Diverse stresses cause transient fluidization of the cytoplasm
- Polysome collapse is required for cytoplasmic fluidization
- mRNA condensation into stress granules or P-bodies is also required
- Cytoplasmic fluidization facilitates the formation of new mesoscale structures

Authors

Ying Xie, Tong Shu, Tiewei Liu, ...,
Glen M. Hocky, David Gresham,
Liam J. Holt

Correspondence

dgresham@nyu.edu (D.G.),
liam.holt@nyulangone.org (L.J.H.)

In brief

Cells must reorganize when exposed to stress. Xie et al. discover that the cytoplasm is initially fluidized in all stress conditions they test. This biophysical change requires polysomes to disassemble and mRNA to condense into P-bodies or stress granules. Fluidization allows for the efficient formation of new stress-induced structures.

Xie et al., 2024, Molecular Cell *84*, 2698–2716
July 25, 2024
https://doi.org/10.1016/j.molcel.2024.06.024

CellPress

CellPress
Molecular Cell

Article

Polysome collapse and RNA condensation fluidize the cytoplasm

Ying Xie,[1,2] Tong Shu,[1] Tiewei Liu,[1,3] Marie-Christin Spindler,[4] Julia Mahamid,[4,5] Glen M. Hocky,[6] David Gresham,[2,*] and Liam J. Holt[1,7,*]
[1]Institute for Systems Genetics, New York University Langone Medical Center, New York, NY, USA
[2]Department of Biology, New York University, New York, NY, USA
[3]Department of Molecular Biology and Genetics, Cornell University, Ithaca, NY, USA
[4]Structural and Computational Biology Unit, European Molecular Biology Laboratory (EMBL), Heidelberg, Germany
[5]Cell Biology and Biophysics Unit, EMBL, Heidelberg, Germany
[6]Department of Chemistry and Simons Center for Computational Physical Chemistry, New York University, New York, NY, USA
[7]Lead contact
*Correspondence: dgresham@nyu.edu (D.G.), liam.holt@nyulangone.org (L.J.H.)
https://doi.org/10.1016/j.molcel.2024.06.024

SUMMARY

The cell interior is packed with macromolecules of mesoscale size, and this crowded milieu significantly influences cellular physiology. Cellular stress responses almost universally lead to inhibition of translation, resulting in polysome collapse and release of mRNA. The released mRNA molecules condense with RNA-binding proteins to form ribonucleoprotein (RNP) condensates known as processing bodies and stress granules. Here, we show that polysome collapse and condensation of RNA transiently fluidize the cytoplasm, and coarse-grained molecular dynamic simulations support this as a minimal mechanism for the observed biophysical changes. Increased mesoscale diffusivity correlates with the efficient formation of quality control bodies (Q-bodies), membraneless organelles that compartmentalize misfolded peptides during stress. Synthetic, light-induced RNA condensation also fluidizes the cytoplasm. Together, our study reveals a functional role for stress-induced translation inhibition and formation of RNP condensates in modulating the physical properties of the cytoplasm to enable efficient response of cells to stress conditions.

INTRODUCTION

The cytoplasm undergoes rapid changes in its physical properties in response to stress. Notably, when ATP or glucose is depleted, the cytoplasm of bacterial and yeast cells can undergo a solid-state transition characterized by a significant reduction in macromolecular motion.[1–3] However, an immediate and uniform slowdown of all cellular processes might not be helpful in all stress conditions since there are many processes that must be coordinated in a time-dependent manner to achieve stress adaptation. For example, stress-responsive transcription factors translocate from the cytosol to the nucleus within minutes of *Saccharomyces cerevisiae* (*S. cerevisiae*) encountering environmental stresses, activating stress response transcription.[4–7] Also, the cell significantly rearranges the plasma membrane,[8] vacuole membrane,[9] and inter-organelle membranes such as nuclear-vacuole junctions[10] in response to glucose starvation. Finally, new structures form within the cytoplasm upon stress. For example, some misfolded proteins are directed to Q-bodies, which are membraneless organelles that form upon heat stress and glucose starvation.[11–14] Formation of Q-bodies depends on the interactions between the HSP42 chaperone and misfolded proteins.[15] This large-scale remodeling of the cell in response to stress is incompatible with an immediate solidification of the cytoplasm. Therefore, more detailed studies of the physical properties of the cytoplasm during the initial response to stress are necessary.

Cells are highly crowded with mesoscale (10 nm–1 μm diameter) particles[16,17] (Figure 1A). Crowding both hinders mesoscale motion and drives assembly of mesoscale structures.[18,19] Active biological processes, such microtubule assembly,[20] also influence the motion of mesoscale particles. Thus, the crowded environment is crucial for efficient cellular functions, but the mechanisms controlling these biophysical factors and their influence on biochemistry are only beginning to be understood.

In a previous study, ribosomes, with a diameter of 25 nm, were identified as dominant mesoscale crowders in the cytoplasm, accounting for approximately half of the total excluded volume (around 20% of the total cytoplasmic volume).[21] Inhibition of the target of rapamycin complex 1 (TORC1) kinase reduced the concentration of ribosomes, thereby decrowding the cytoplasm, which both increased the diffusivity of mesoscale particles and influenced the formation of phase-separated condensates.[21] However, actively translating ribosomes are further

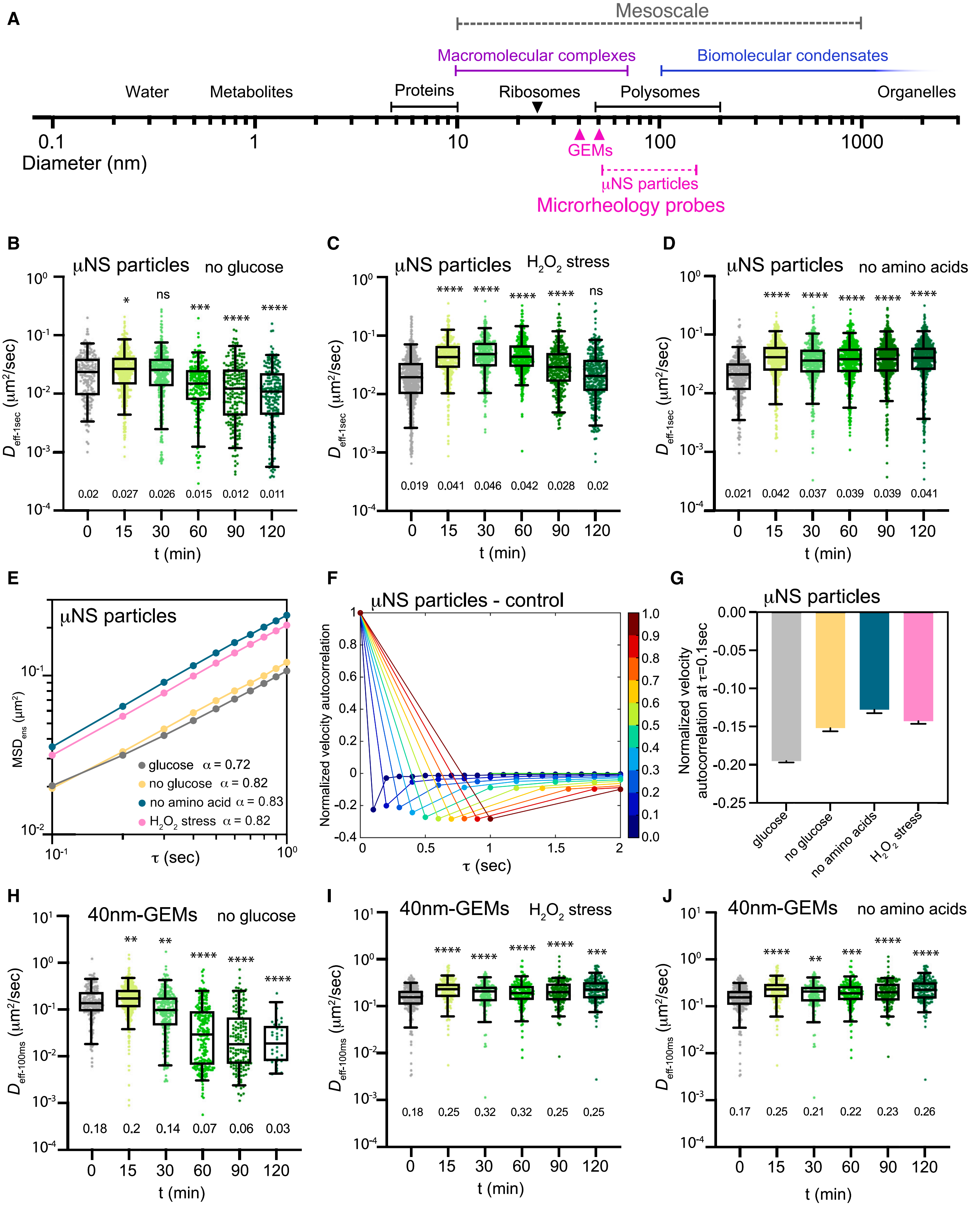

(legend on next page)

organized into polysome complexes, which vary in size depending on the number of ribosomes bound to the mRNA. These higher-order cytoplasmic structures might create elastic confinement that could restrict diffusivity of mesoscale particles.

In response to many environmental stresses, there is a general suppression of protein production, primarily by inhibiting the rate-limiting step of translation initiation.[22–24] In both yeast and mammalian cells, multiple stresses, including glucose starvation, amino acid starvation, and oxidative stress, trigger a significant reduction of translation within minutes, leading to disassembly of polysome complexes into monosomes and the release of mRNA.[25–27] The mRNA released from polysomes upon stress is rapidly bound by proteins and forms ribonucleoprotein (RNP) condensates, including stress granules (SGs) and processing bodies (P-bodies).[28,29] These condensates vary in size from 100 nm to microns in diameter depending on the stress condition and cell type,[30,31] some of which are diffraction-limited and therefore undetectable by conventional light microscopy.[31–34] Polysomes and mRNA are extremely abundant in the cytoplasm, and therefore changes in the assembly state of ribosomes (from polysomes to monosomes) and the redistribution of mRNA to RNP condensates could impact the biophysical properties of the cytoplasm.

Here, we investigated mesoscale particle diffusivity in the period immediately following acute stresses in both yeast and mammalian cells. We discovered a transient increase in mesoscale cytoplasmic diffusivity in all stress conditions tested. The collapse of polysome complexes was a prerequisite for this fluidization. However, polysome collapse was not sufficient; in addition, the condensation of released mRNA into P-bodies or SGs was also required. In yeast cells, this fluidization of the cytoplasm was required for the efficient formation of Q-body condensates. Our findings provide new insights into how polysome collapse and RNA condensation influence the biophysical properties of cells, allowing for efficient mesoscale reorganization of the cell.

RESULTS

Mesoscale diffusivity transiently increases upon diverse types of stresses

Microrheology is the inference of the physical properties of a material from the observation of the motion of passive probes embedded within the environment.[35] Passive rheological probes have proven to be effective tools for inferring the biophysical properties of different cellular compartments.[1,3,21,36–39] Previous reports have described decreased motion of mesoscale particles upon acute glucose starvation.[2] However, these observations monitored diffusivity of mRNP probes, which were later found to strongly interact with P-bodies, preventing the inference of general cytoplasmic properties from changes in their diffusivity.[40] Furthermore, our recent study using passive rheological probes identified increased mesoscale diffusivity upon acute glucose starvation.[41] To follow up on this observation, we sought to characterize the dynamics and mechanisms underlying this change by expanding our analysis to include additional time points. In addition, we investigated physical properties of the cytoplasm at two length scales by using both μNS particles (with a diameter of 50–150 nm; μNS is a subdomain of an avian reovirus protein that forms condensates)[1] and genetically encoded multimeric nanoparticles with a diameter of 40 nm, hereafter 40nm-GEMs).[21]

As the cytoplasm does not satisfy the simplifying assumptions of the Stokes-Einstein equation,[19,42,43] it is not possible to assign a single diffusion constant for a particle. Rather, the effective diffusivity of particles must be assigned at a specific timescale. We chose a timescale of 100 ms ($D_{\text{eff-100ms}}$) for 40nm-GEMs and 1 s ($D_{\text{eff-1s}}$) for μNS particles because the step-size distribution of these particles was similar to each other at these time intervals (Figures S2A and S2B).

In agreement with our recent results,[41] we found a transient increase in the $D_{\text{eff-1s}}$ of μNS particles immediately after glucose starvation that was most significant at the earliest time point that we assayed (15 min) and returned to initial values after 1 h (Figure 1B). Note, we were careful to osmotically balance all media and confirmed that there was no significant change of cytosolic volume upon acute glucose starvation (Figure S1). We then examined two additional stress conditions—oxidative stress with H_2O_2 and amino acid starvation—and found that both stresses caused increased diffusivity of μNS within 30 min (Figures 1C and 1D). Interestingly, the subsequent dynamics of mesoscale diffusivity varied between stresses: in glucose starvation, diffusivity ultimately decreased below initial values; after oxidative stress, diffusivity ultimately returned to initial values; and after amino acid starvation, diffusivity remained high even after 2 h (Figures 1B–1D).

The anomalous exponent α value of μNS particles was consistent with sub-diffusive motion ($\alpha < 1$, Figure 1E). Anomalous

Figure 1. Diverse stresses lead to a transient increase in diffusivity of mesoscale particles

(A) Mesoscale rheological probe sizes in relation to biological length scales.

(B–D) The effective diffusivity at 1 s ($D_{\text{eff-1s}}$), $\log_{10}$ scale, for μNS particles after acute glucose starvation (left), oxidative H_2O_2 stress (middle, synthetic complete medium with 2% glucose and 0.3 mM H_2O_2 as oxidative stress), and acute amino acid starvation (right, media with 2% glucose and no amino acids) in *S. cerevisiae* cells. Each datapoint represents one cell. $N = 3$ biological replicates, $n > 100$ cells. Boxes represent the 5%–95% confidence interval; median value is indicated below each box. All p values were determined by one-way ANOVA; ns, not significant; $^*p < 0.05$, $^{***}p < 0.001$, $^{****}p < 0.0001$.

(E) Ensemble-averaged mean-squared displacement (MSD) versus time delay (τ), $\log_{10}$ scale. A linear model was fit to determine the anomalous exponent α values for μNS particles in the indicated conditions at 30 min (glucose: $n = 10{,}437$ trajectories; no glucose: $n = 16{,}372$ trajectories; no amino acids: $n = 1{,}589$ trajectories; H_2O_2 stress: $n = 558$ trajectories).

(F) Normalized velocity autocorrelation with respect to $\tau = 0$ s for μNS particles, with correlations calculated over different tracking time intervals (0–1 s, blue to red) for WT yeast cells in glucose-rich medium.

(G) Summary of velocity autocorrelation values at $\tau = 0.1$ s for various conditions at 30 min in WT yeast cells. Error bars are standard deviation (SD).

(H–J) Effective diffusivity at 100 ms ($D_{\text{eff-100ms}}$), $\log_{10}$ scale, for 40nm-GEMs upon acute glucose starvation, acute amino acid starvation, and H_2O_2 stress in *S. cerevisiae* cells. Each data point represents one cell. $N = 3$ biological replicates, $n > 100$ cells. Boxes represent the 5%–95% confidence interval; median value is indicated below each box. All p values were determined by one-way ANOVA; $^{**}p < 0.01$, $^{***}p < 0.001$, $^{****}p < 0.0001$.

subdiffusion can arise for multiple reasons. We found that mean-square displacement does not reach a plateau over the timescale of the experiment, suggesting the μNS particles are unlikely to be under rigid confinement. Other possible reasons for subdiffusion include interactions with the environment and elastic confinement. Elastic confinement gives rise to specific forms of time-correlated motion.[44] μNS particle trajectories have a negative velocity autocorrelation on short timescales, consistent with elastic memory (Figure 1F; Figures S2D–S2G). The value of this autocorrelation was variable depending on timescale, again consistent with elastic behavior rather than rigid confinement (Figure 1F; Figures S2D–S2G).[44] To simplify visualization, we focused on a single tracking timescale to compare multiple conditions ($\tau = 0.1$ s) (Figure 1G). In wild-type (WT) cells, we observed that the negative velocity autocorrelation value was diminished in all three stress conditions, suggesting that elastic confinement was decreased (Figure 1G).

40nm-GEMs also displayed a transient increase in $D_{\text{eff-100ms}}$ after 15 min of glucose starvation and maintained high mesoscale diffusivity in both amino acid starvation and oxidative stress with H_2O_2 (Figures 1H–1J). However, the anomalous exponent α value of 40nm-GEMs remained around 1 in all tested stresses, suggesting that these smaller particles experience less elastic confinement (Figure S2C). Again, the elastic confinement varied depending on timescale, but we do not find obvious differences between control and stress conditions (Figures S2H–S2K).

ATP levels and pH decrease upon glucose starvation

The physical properties of the cytoplasm undergo complex changes over time following glucose withdrawal: first mesoscale diffusivity increases, but later it decreases. Budding yeast are adapted to acidic environments, and the plasma membrane ATPase (PMA1) uses large amounts of ATP to pump out protons and maintain a near-neutral intracellular pH[2,45]. This pump inactivates during starvation to conserve energy, and consequently, both ATP levels and pH decrease upon glucose withdrawal.[2,46] We used the ratiometric fluorescent ATP sensor, namely quantitative evaluator of cellular energy (QUEEN),[47,48] and the ratiometric pH sensor pHluorin[49] to quantify ATP levels and intracellular pH. We found that ATP levels plummet within 10 min of acute glucose starvation (Figures S3A and S3B), while intracellular pH reduced to 6.6 from the log-phase value of 7.7 after 10 min of glucose starvation and fell to 6.3 after 30 min of glucose starvation, consistent with earlier reports (Figures S3C and S3D). Previous studies have shown that ATP depletion experiments in media without glucose and supplemented with 2-deoxyglucose (2-DG, an inhibitor of glycolysis) and antimycin A (an inhibitor of mitochondrial respiration) in an acidic environment drastically reduces movement of endogenous particles as well as μNS particles after 2 h treatment.[3] We performed the same drug treatments for ATP depletion experiments in media buffered at pH 5.5 without glucose and measured particle motion at several additional early time points. Consistent with previous results, we found that both μNS particles and 40nm-GEMs displayed a reduction in effective diffusivity and a shift to smaller step sizes after 30 min (Figures S3E–S3G). These results suggest that decreases in pH and ATP drive the ultimate decrease in diffusivity after an hour of glucose starvation. However, the initial increase of mesoscale diffusivity is likely to be due to other intracellular changes. We sought to identify those factors.

Disassembly of polysomes is required for increased cytoplasmic fluidity

In the cytoplasm, ribosome concentration is a major determinant of mesoscale particle diffusivity. Inhibition of TORC1 signaling reduces ribosome concentration and leads to increased diffusivity of mesoscale particles.[21] However, this change relies on autophagy and takes more than 1 h. We observe increased diffusivity and decreased elastic confinement after less than 15 min of acute stress. Therefore, we hypothesized that other properties of ribosome physiology could explain the rapid fluidization of the cytoplasm upon acute glucose starvation and other stresses.

In rapidly proliferating yeast cells, more than 80% of ribosomes are engaged in protein translation[50,51] often with multiple ribosomes simultaneously translating one mRNA, resulting in polysome complexes (polysomes).[52–54] Upon acute glucose starvation, various mechanisms rapidly inhibit translation initiation, leading to disruption of polysomes.[24] Ribosomes dissociate from mRNA, disassembling into 40S and 60S ribosomal subunits,[25] and then rapidly reassemble into 80S monosomes in an STM1-dependent process.[55,56] We hypothesized that collapse of polysomes might transiently fluidize the cytoplasm in stress conditions.

Consistent with previous studies,[25] polysome profiling by fractionation of cell extracts on a sucrose gradient indicated a dramatic reduction in the fraction of ribosomes in polysomes within minutes of acute glucose starvation (Figures 2A and 2B). Our hypothesis predicts that preventing polysome disassembly should prevent cytoplasmic fluidization. To test this prediction, we treated cells with cycloheximide, which freezes translation elongation, prevents ribosome dissociation from mRNAs, and therefore prevents polysome collapse[57] (Figures 2A and 2C). Consistent with our prediction, simultaneous stress and cycloheximide treatment completely abolished the increase in diffusivity of μNS particles (Figure 2D). By contrast, cycloheximide treatment in glucose-rich medium did not change the diffusivity of μNS particles (Figure 2D), suggesting that inhibition of translation elongation per se does not impact cytoplasmic fluidity, but rather changes in polysome abundance are crucial. Furthermore, preventing polysome disassembly also prevented the reduction of elastic confinement in all tested stresses (Figure 2E). Therefore, we conclude that polysome disassembly is crucial for the initial transient increase of mesoscale particle diffusivity and reduction of elastic confinement (Figures 2D and 2E).

To better understand the spatial constraints imposed by polysomes, we analyzed their distribution within cells by cryoelectron tomography (cryo-ET) of *S. cerevisiae* (Figure 2F; Figures S4A–S4E; STAR Methods[58,59]). To define polysomes, we detected ribosomes in the cryo-ET data of cells in glucose-rich and acute glucose-starvation conditions and measured the distance between the mRNA exit and entry sites between adjacent ribosomes, taking their refined relative orientations into account (Figure S4F). In glucose-rich conditions, the distances exhibited a bimodal distribution that could be fit by two Gaussians, while

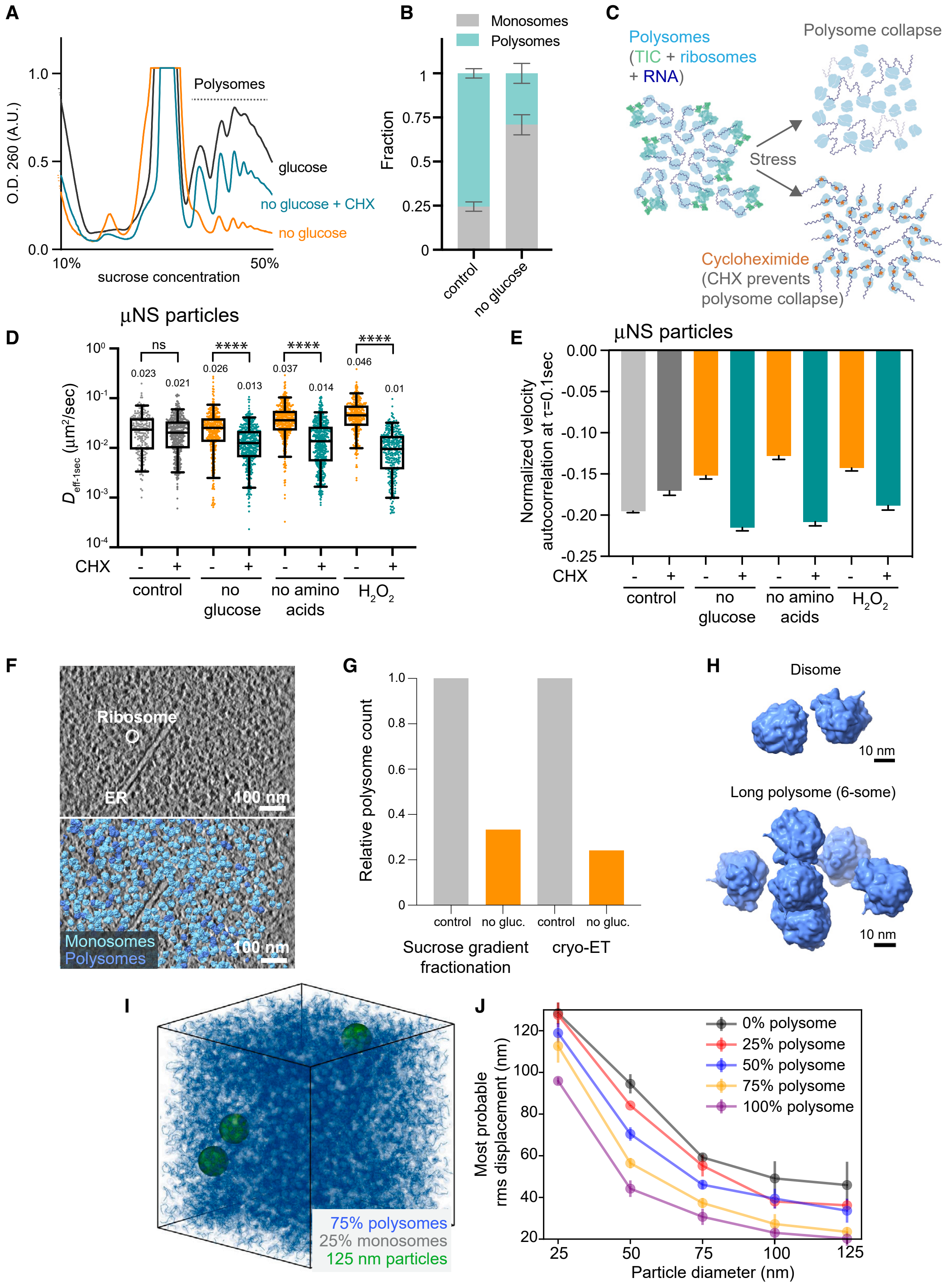

(legend on next page)

the peak around smaller distances was largely absent upon glucose starvation. We used a conservative exit to entry site distance cutoff of 8 nm to assign pairs of ribosomes into a class of closely assembled polysomes (Figures S4G and S4H). This analysis assigned 18.6% of ribosomes to polysomes in glucose-rich conditions. After 30 min of acute glucose starvation, the polysome fraction was reduced to 4.5%. These values are smaller than those estimated from biochemical fractionation (Figure 2B) as polysomes with loosely packed arrangements are not detected and thus not included in the cryo-ET data analysis. Therefore, to compare the change in polysome fraction upon glucose starvation determined by sucrose gradient fractionation and the cryo-ET data, we normalized the number of polysomes in the starvation conditions to the respective glucose controls (Figure 2G). Both experiments showed a similar decrease in polysome fractions with a reduction of 67% based on sucrose gradient fractionation and 76% based on the cryo-ET data. Consistently, maps generated by subtomogram averaging of the ribosomes exhibited clear densities at the mRNA exit and entry sites under the glucose-rich conditions that are indicative of polysomal arrangement, and which were not present in the starvation condition (Figure S4I). Furthermore, the size of polysomes decreased under glucose starvation (Figure 2H; Figure S4J). The overall reduction in polymeric crowders and shift to smaller polysome sizes under glucose starvation is consistent with our hypothesis that a disassembly of polysomes due to short-term glucose starvation promotes mesoscale fluidization.

We next developed a coarse-grained molecular dynamics (CGMD) simulation to test whether the presence of polysomes could be sufficient to explain the changes in mesoscale particle dynamics that we observed experimentally (Figure 2I). We parameterized our simulation based on the fraction of polysomes and monosomes determined by sucrose gradient fractionation (Figure 2B) and the 30% excluded volume fraction in the cytoplasm measured previously.[21] Polysomes were represented as a chain of six connected ribosomes, to match the median polysome length measured in our sucrose gradient ribosome profiles (Figure 2A). Representative renderings of these simulations are shown in Videos S1 and S2. We then modeled the effect of changes in polysome fraction on the effective diffusivity of particles of various sizes and found that increasing the fraction of polysomes reduced mesoscale particle diffusivity in a size-dependent manner (Figure 2J), consistent with our experimental findings.

Condensation of RNA into SGs or P-bodies is required for cytoplasmic fluidization

Upon polysome disassembly, mRNAs are released. These mRNA molecules can associate with RNA-binding proteins that drive the formation of stress-induced condensates, including P-bodies and SGs[60–62] (Figure 3A). The release of mRNA and formation of these condensates is blocked by cycloheximide.[63] We hypothesized that, upon release from polysomes, free mRNA molecules could contribute to interactions that increase the elasticity of the cytoplasm, and condensation of mRNAs might reduce these interactions and thereby reduce elastic confinement.

To test this hypothesis, we monitored the formation of RNP granules in cells challenged by stresses through live-cell imaging of the Dcp2 and Pab1 proteins, which are markers for P-bodies and SGs respectively (Figure 3B). Consistent with previous reports,[60] P-bodies formed rapidly, becoming clearly visible 10 min after acute glucose starvation, while visible SGs appeared more slowly and were less prominent (Figure 3B). Treatment with cycloheximide completely inhibited the formation of both P-bodies and SGs (Figure 3B). On the other hand, we observed Dcp2 foci but not Pab1 foci in both amino acid starvation and oxidative stress (Figure S5A), suggesting that P-bodies are formed in these conditions and that if SGs are formed, they are diffraction-limited and not readily detected by conventional light microscopy.[31,34]

Since the formation of RNP granules correlated with cytoplasmic fluidization, we tested if these structures are required

Figure 2. Polysome disassembly is necessary for increased mesoscale diffusivity in response to stress

(A) Polysome profile analysis by fractionation of cell extracts on a sucrose gradient. Cells were collected 30 min after switching to the indicated conditions (CHX: 100 μg/mL cycloheximide just prior to glucose starvation).

(B) Quantification of polysome profiles: the area under the curve was used to determine the relative amounts of 80S monosomes and polysomes. $N = 3$ biological replicates. Error bars are standard error of the mean (SEM).

(C) Schematic of polysome rearrangement upon acute glucose starvation with or without cycloheximide. Green: translation initiation complexes (TICs); cyan: ribosomes; dark blue: RNA; orange: cycloheximide.

(D) Effective diffusivity at $\tau = 1$ s ($D_{\text{eff-1s}}$) for μNS particles after pretreatment with cycloheximide followed by 30 min in normal glucose, acute glucose starvation, acute amino acid starvation, or H_2O_2 stress in *S. cerevisiae* cells. Each datapoint represents one cell. $n > 100$ cells, $N > 3$ biological replicates for each condition. Boxes represent the 5%–95% confidence interval; median value is indicated above each box. *p* values were determined by one-way ANOVA; ns, not significant; $^{****}p < 0.0001$.

(E) Normalized velocity autocorrelation at tracking $\tau = 0.1$ s after 30 min in the indicated conditions in WT yeast cells, with or without 100 μg/mL cycloheximide. Error bars are SD.

(F) A tomographic slice from *S. cerevisiae* in control glucose medium (top: the cytoplasm is crowded with dense globular ribosomes; single ribosomes encircled; ER, endoplasmic reticulum) and overlaid with 3D rendering of monosomes (bottom, light blue) and polysomes (dark blue) annotated based on refined positions and orientations derived from subtomogram averaging in 3D. Scale bar: 100 nm.

(G) Polysome counts at 30 min acute glucose starvation as a fraction of the polysome counts in the control condition for sucrose gradient fractionation and cryo-ET data.

(H) Representative 3D annotations of a short (disome) and long (6-some) polysome. Scale bar: 10 nm.

(I) Representative image of coarse-grained molecular dynamics (CGMD) framework. In this example, ribosomes occupy 30% of total box volume, 75% of which are modeled as polysomes (dark blue) and 25% as monosomes (gray), 125-nm particles are shown in green.

(J) The most probable root mean squared (RMS) displacement after t = 100 simulation time units for particles of various sizes simulated with 0%, 25%, 75%, and 100% ribosomes as polysomes. Error bars are SD; $N = 5$.

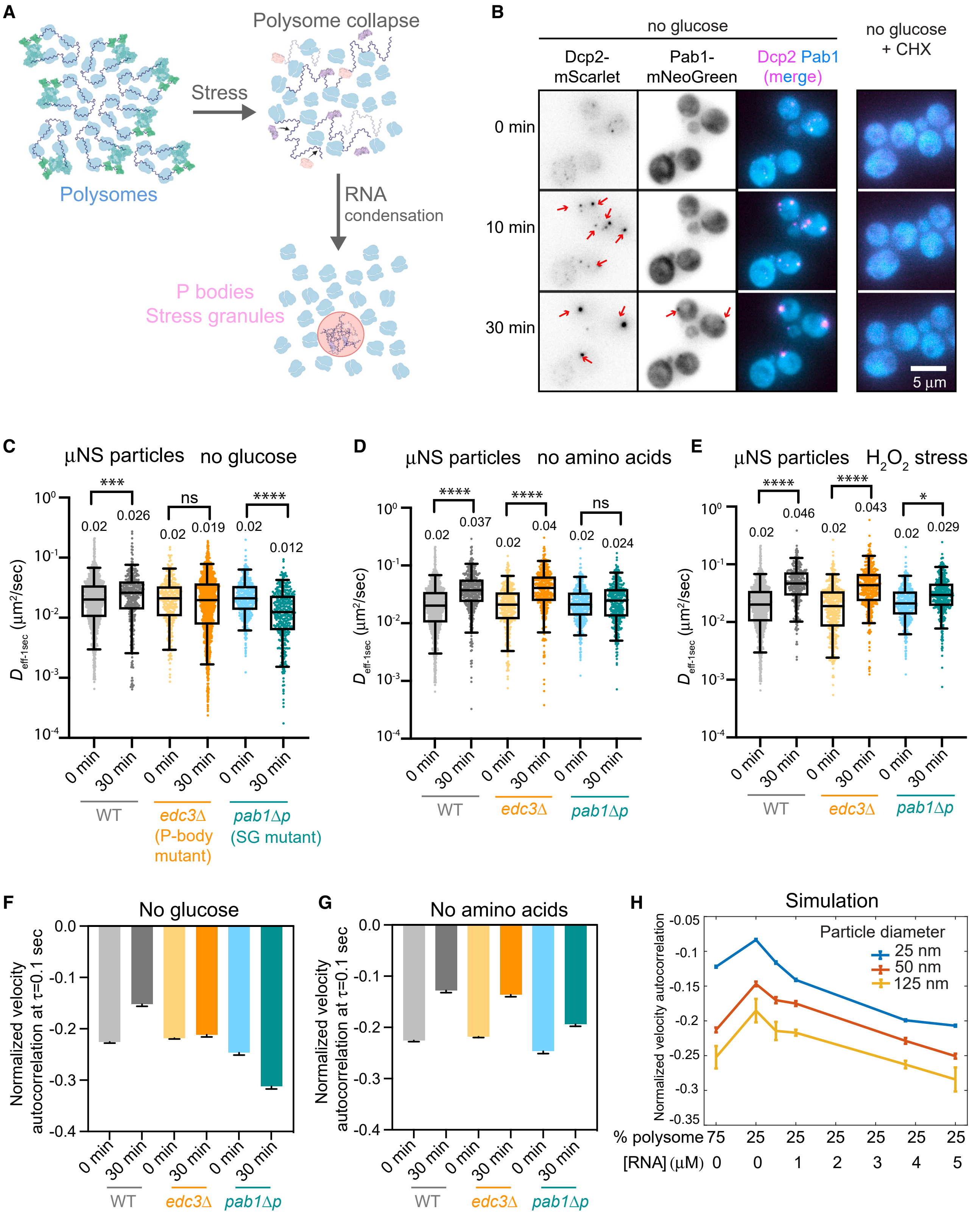

(legend on next page)

for this physical change. The Edc3 protein is a key P-body scaffold.[64–66] We found that an *EDC3* gene deletion mutant (*edc3Δ*) failed to efficiently form P-bodies in all tested stresses, as indicated by a marked reduction in the appearance of Dcp2 foci (Figures S5B–S5D). To inhibit SG formation, we used *pab1ΔP* mutant cells.[67] The low complexity P domain has been demonstrated to facilitate Pab1 protein phase separation *in vitro*, and *pab1ΔP* mutant cells have reduced cellular fitness in heat stress and energy depletion stress.[67] First, we confirmed that neither rheological probe was sequestered into P-bodies upon acute glucose starvation (Figures S5E and S5F), making us confident that they were reliable reagents for defining the cytosolic environment outside of P-bodies. We observed almost no increase of μNS particle diffusivity in *edc3Δ* mutant cells and a decrease of μNS particle diffusivity in *pab1ΔP* after 30 min of glucose starvation (Figure 3C). Analysis of the normalized velocity autocorrelation function also showed no reduction in elastic confinement in these mutants (Figure 3F). Furthermore, *pab1ΔP* abrogated or strongly attenuated mesoscale fluidization in both amino acid starvation and H_2O_2 treatment (Figures 3D–3G), highlighting a crucial role for SGs assembly in driving mesoscale fluidization of the cytoplasm in these stresses. Thus, P-bodies are required for cytoplasmic fluidization in glucose starvation, and SGs are required for cytoplasmic fluidization in all stresses that we tested.

Our experimental data strongly support a model in which both polysomes and mRNAs in the cytosol can contribute to elastic confinement that limits mesoscale diffusivity. To independently test the biophysical role of polysome concentration and free mRNA, we built upon our simulation framework. As a minimal change to our model, we included free RNA as spherical particles that have a weak nonspecific interaction with ribosomes. To parameterize the simulation, we chose polysome and RNA concentrations based on our measurements and those reported in the literature (Figure 2B). Specifically, it has been reported that there are 15,000–60,000 mRNAs per yeast cell,[68,69] and the yeast cytoplasmic volume is around 25 μm^3 (Figure S1D), which corresponds to a cytoplasmic mRNA concentration of 1–4 μM. We measured the normalized velocity autocorrelation function to infer elastic confinement in our simulations. 125 nm particles displayed negative velocity autocorrelations that were most apparent at short timescales (Figures S5G–S5I; Videos S1, S2, and S3). Consistent with our experimental results, we found that both high polysome fractions and the presence of free RNA increased elastic confinement of these mesoscale particles (Figure 3H).

Increased mesoscale diffusivity facilitates Q-body formation upon acute glucose starvation

Multiple types of membraneless organelle form in stress conditions,[13,29,30,70,71] often by an initial nucleation of multiple small assemblies that then fuse together to form the mature organelle. This growth by coalescence can be inhibited by crowded or elastic confined environments because subassemblies reach a size at which they no longer diffuse efficiently to encounter one another and fuse. For example, the growth of synthetic condensates is mechanically inhibited by chromatin,[72] and the cytoplasm has been shown to have elastic properties that frustrate the growth of synthetic mesoscale condensates.[18] We therefore hypothesized that the fluidization of the cytoplasm by polysome disassembly and RNP granule formation could facilitate the formation of other mesoscale membraneless organelles.

Q-bodies are membraneless organelles that form upon glucose starvation or heat shock. These acute stresses abruptly terminate protein translation, likely leading to accumulation of nascent peptides that may misfold.[73] At the same time, a sudden drop of ATP levels can cause formation of protein aggregates in cells.[14,74] The chaperone Hsp42 has been demonstrated to associate with misfolded proteins and promote Q-body formation. Deletion of the *HSP42* gene reduces Q-body assembly and reduces cellular fitness when yeast cells are challenged by heat stress or glucose starvation,[11,14] indicating that Q-bodies help cells adapt to stress.

We tested if transiently increased mesoscale diffusivity upon glucose starvation was important for efficient Q-body assembly. We used endogenously tagged Hsp42-mScarlet to indicate Q-body assembly and measured μNS diffusivity 15 min after glucose starvation and the subsequent intensity of Hsp42 foci 75 min after glucose starvation in the same cells. We found significant positive correlation between early cytoplasmic fluidization and the intensity of Hsp42 foci (Figures 4A and 4B). These results suggest that cytoplasmic fluidization may enable Q-body assembly.

We then compared Q-body formation upon acute glucose starvation between WT and *edc3Δ* (P-body deficient) mutants (Figures 4C and 4D). In WT cells, we found that the average number of Hsp42-mScarlet foci increased over the first hour of glucose starvation until, on average, all cells had one Q-body (Figure 4D, black line) Thus, Q-body formation occurs during the period of transient fluidization of the cytoplasm after glucose starvation. Strikingly, Q-body formation was significantly attenuated in the *edc3Δ* mutants that do not effectively fluidize their cytoplasm (Figures 4C and 4D, orange line), consistent with

Figure 3. Formation of SGs and P-bodies is required for mesoscale fluidization of the cytoplasm

(A) Schematic of P-body and SG formation. Green: translation initiation complexes; cyan: ribosomes; dark blue: RNA; pink: RNA-binding proteins.

(B) Representative images of cells with P-body (Dcp2-mScarlet) and SG (Pab1-mNeoGreen) markers during acute glucose starvation. Cycloheximide (CHX) pretreatment inhibits the formation of both RNP condensates. Scale bar: 5 μm.

(C–E) The effective diffusivity at 1 s ($D_{eff\text{-}1s}$) for μNS particles in *S. cerevisiae* cells. Each datapoint represents one cell. $n > 100$ cells, $N = 3$ replicates for each condition. Boxes represent the 5%–95% confidence interval; median value is indicated above each box. *p* values were determined by one-way ANOVA; ns, not significant; $^{*}p < 0.05$, $^{***}p < 0.001$, $^{****}p < 0.0001$.

(F and G) Values at $\tau = 0.1$ s for normalized velocity autocorrelation were extracted for the indicated conditions upon 30 min treatment in WT, edc3Δ, and *pab1ΔP* yeast cells. Error bars are SD.

(H) Normalized velocity autocorrelations at the first simulation time unit for all indicated simulation conditions. The total volume occupied by ribosomes (polysomes and monosomes) is 30%. "Normal growth conditions" were simulated as 75% polysomes, 25% monosomes, with no free RNA. "Glucose-starvation conditions" were simulated as 25% polysomes, 75% monosomes, with varying concentrations of free RNA (from 0 to 5 μM). Error bars are SD.

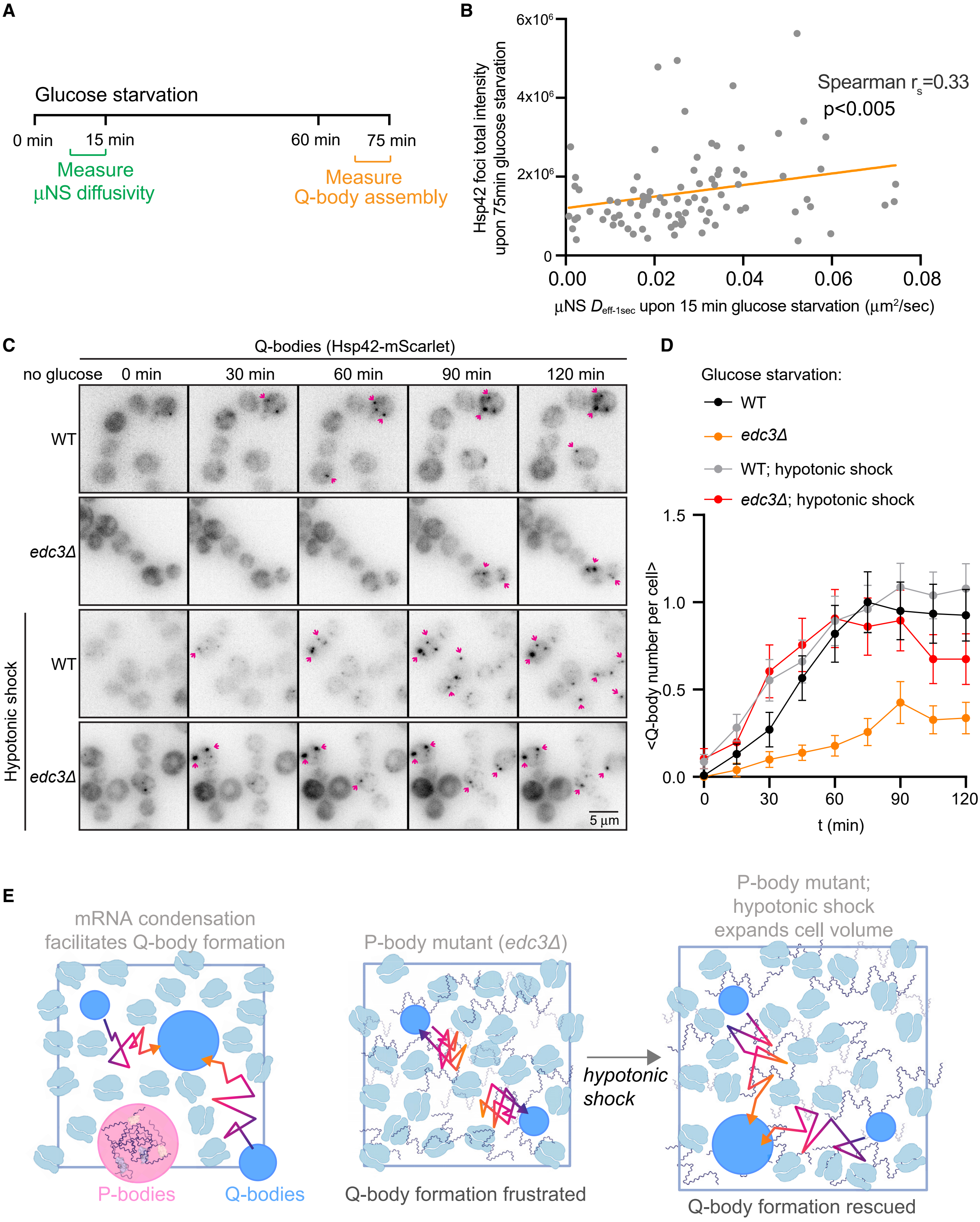

(legend on next page)

cytoplasmic fluidization enabling formation of mesoscale Q-bodies.

An alternative hypothesis is that *Edc3* or P-bodies are required for Q-body formation through a mechanism independent of cytoplasmic fluidization. If physical fluidization of the cytoplasm is the key defect in *edc3Δ* cells, orthogonal methods to fluidize the cytoplasm should rescue Q-body formation. It is possible to decrowd the cytoplasm by increasing cell volume through acute hypotonic shock.[21] To achieve hypotonic shock, we cultured WT and *edc3Δ* mutant yeast cells in hypertonic media (media supplemented with 500 mM KCl as an osmolyte) overnight. In these conditions, cells activate the high-osmolarity glycerol (HOG) pathway to accumulate osmolytes (primarily glycerol), thereby osmotically balancing the cell interior enabling growth.[75] Suddenly shifting these cells to media without excess osmolyte (i.e., without KCl) creates a hypotonic shock because the osmolytes that have accumulated in the cell take time to be degraded and exported.[76] This hypotonic shock causes water to enter the cell, leading to a sudden increase in volume and a corresponding decrease in macromolecular crowding, thereby increasing mesoscale diffusivity.[21]

Upon hypotonic shock, the diffusivity of μNS particles increased drastically at 5 min in both WT and *edc3Δ* mutant cells, without changing the size of μNS particles (Figures S6A–S6C). Consistent with our hypothesis, experimentally induced decrowding of the cytoplasm was sufficient to completely rescue Q-body assembly in *edc3Δ* cells (Figures 4C and 4D, red line).

We confirmed that there is no translation defect in *edc3Δ* cells in normal growth conditions, and a similar reduction of polysomes was observed in *edc3Δ* cells compared with WT yeast in glucose starvation (Figures S6D–S6F), consistent with previous reports.[64] Based on these observations, we conclude that the reduction of microscopically visible P-bodies in an *edc3Δ* mutant was not due to defects in translational repression, but rather due to the failure to condense untranslated mRNAs into P-bodies. Furthermore, neither hypotonic shock nor deletion of *EDC3* affected ATP levels over the course of these experiments; we observed the same degree and kinetics of ATP reduction during starvation compared with WT cells (Figures S6G–S6J). Finally, we confirmed that the P-body assembly defect was still present in *edc3Δ* cells upon glucose starvation in the hypotonic shock condition (Figures S6K and S6L). These results support our model in which P-body formation increases mesoscale particle diffusivity, facilitating the formation of mesoscale Q-body condensates during the initial response to glucose starvation (Figure 4E).

SG formation increases mesoscale diffusivity in mammalian cells

In mammalian cells, SGs are induced in response to diverse stresses.[29,77–80] G3BP1 and G3BP2 proteins are important scaffolds for SG formation that interact with both RNA and RNA-binding proteins.[79,80] Cells with a double knockout (dKO) of *G3BP1* and *G3BP2* (*G3BP1/2 dKO*) were previously demonstrated to prevent SG formation in some types of stress such as sodium arsenite but not others, such as heat stress.[79] Therefore, we analyzed how mesoscale diffusivity was impacted by sodium arsenite treatment and 45°C heat stress using human bone osteosarcoma epithelial (U2OS) cells. Note that the μNS particles that we used as rheology probes in yeast cells were originally derived from a vertebrate viral protein,[81] and so we were not confident that these could be used as passive orthogonal probes in mammalian cells; therefore, we restricted our mammalian experiments to GEM nanoparticles. There was an increased variance of the median diffusivity of 40nm-GEMs between control cells after heat shock that was not apparent in *G3BP1/2 dKO* cells (Figures 5A and 5B). These results suggest that SGs impact the physical properties of cells in complex ways in the context of heat shock that will require further study to understand. On the other hand, we found that the diffusivity of 40nm-GEMs increased after 30 min of oxidative stress induced by 100 μM sodium arsenite in control cells but not *G3BP1/2 dKO* cells (Figure 5A), consistent with the hypothesis that formation of SGs leads to cytoplasmic fluidization upon oxidative stress.

In general, external stresses lead to translational inhibition and therefore induce SG formation. However, stresses such as heat shock may have pleiotropic effects. Therefore, to more specifically investigate the effects of SGs on the physical properties of the cytoplasm, we used translation inhibitors (Figure 5C). Translation inhibitors that cause collapse of polysomes and release of mRNA (i.e., puromycin causes premature chain termination, and des-methyl, des-amino pateamine A [DMDA]-pateamineA [DMDA-PatA] inhibits the eukaryotic initiation factor-4A [eIF4A]),[82–85] induced widespread formation of SGs as indicated by condensation of the SG protein G3BP1 (Figure S7A). By contrast, treatment with the translation inhibitor cycloheximide, which prevents polysome disassembly,[57] did not lead to SG formation (Figure S7A). Moreover, pretreatment with cycloheximide before applying puromycin or DMDA-PatA suppressed SG formation (Figure S7A), supporting the idea that release of mRNAs from polysomes seeds the formation of SGs.

We analyzed the spatial distribution of mRNAs after triggering SG formation with DMDA-PatA using poly(dT) fluorescence *in*

Figure 4. Increased mesoscale diffusivity is crucial for Q-body assembly upon acute glucose starvation

(A) Timeline for experiments to correlate early μNS particle tracking (at 10–15 min) with Q-body assembly measurement (at 70–75 min) in the same yeast cell.

(B) Correlation between effective diffusivity for μNS particles ($D_{\text{eff-1s}}$) 15 min after acute glucose starvation with the total intensity of Hsp42 foci in the same cell 75 min after acute glucose starvation (n = 128 cells).

(C) Representative images of the dynamics of Q-body formation as indicated by Hsp42-mScarlet in WT and *edc3Δ S. cerevisiae* cells after acute glucose starvation. Hypotonic shock was achieved by overnight culture of yeast cells in synthetic complete media with 2% glucose and 500 mM KCl to log phase (optical density [OD] 600 nm < 0.4) and then switching to glucose-starvation media with no KCl. Scale bar: 5 μm.

(D) Average number of Hsp42 foci per cell after acute glucose starvation in the indicated conditions (WT glucose: n = 122 cells; *edc3Δ* glucose: n = 101 cells; WT glucose, hypotonic shock: n = 103 cells; *edc3Δ* glucose, hypotonic shock: n = 86 cells, N = 3 biological replicates on independent days, mean ± SEM).

(E) Graphic illustration of Q-body assembly. Cyan: ribosomes; dark blue: RNA; pink: P-body; light blue: Q-bodies.

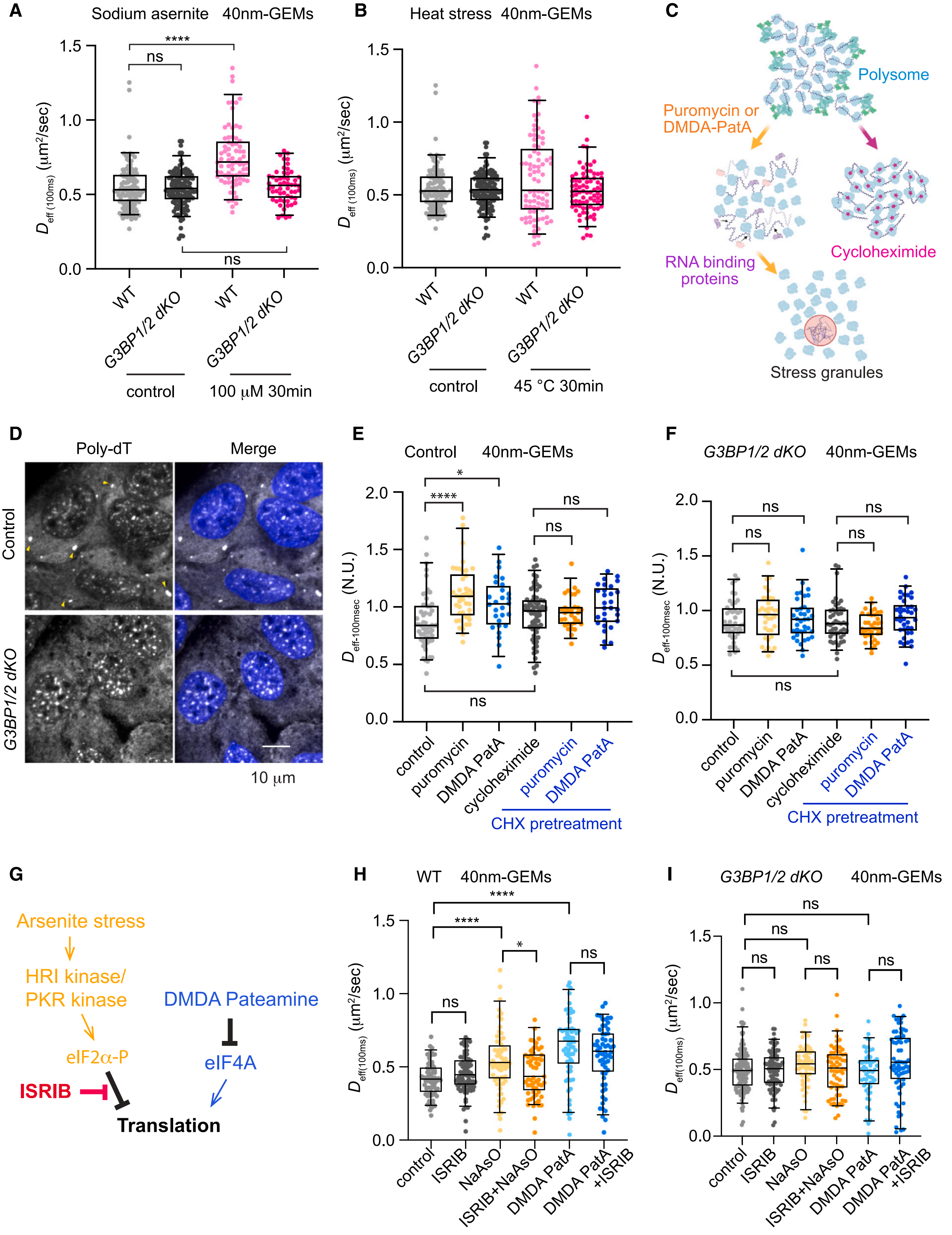

(legend on next page)

situ hybridization (FISH). In U2OS control cells, we observed clear poly(dT) foci in the cytoplasm after DMDA-PatA treatment, consistent with mRNA condensation into SGs (Figure 5D). These poly(dT) clusters were absent in *G3BP1/2 dKO* cells (Figure 5D; Figures S7B and S7C). Together, these results support the model that mRNA released from polysomes upon translation inhibition condenses into SGs in mammalian cells.

Upon puromycin and DMDA-PatA treatment, 40nm-GEMs showed an increase of diffusivity in control U2OS cells but not in *G3BP1/2 dKO* cells (Figures 5E and 5F; Figure S7D). Cycloheximide pretreatment of cells suppressed this effect (Figures 5E and 5F; Figure S7D). Therefore, conditions that lead to formation of SGs cause increased mesoscale particle diffusivity, while preventing SG formation abolishes this physical change.

We expanded our investigation to explore the effects of SG formation on mesoscale diffusivity. SG formation in mammalian cells can be triggered either through the eukaryotic initiation factor 2 (eIF2) phosphorylation (e.g., after sodium arsenite treatment) or inhibition of eIF4A helicase (e.g., DMDA-PatA is an inhibitor of eIF4A). A small molecule named integrated stress response inhibitor (ISRIB) has been developed to attenuate the integrated stress response. ISRIB inhibits SG formation by modifying the effects of eIF2 phosphorylation[86] (Figure 5G). However, ISRIB fails to prevent SG formation upon inhibition of eIF4A helicase activity[87] (Figure 5G). As predicted by our model that SG formation leads to fluidization of the cytoplasm, addition of ISRIB suppressed the increase in diffusivity upon sodium arsenite treatment, but not upon DMDA-PatA treatment in control cells (Figure 5H). By contrast, the physical changes were not observed in *G3BP1/2 dKO* cells (Figure 5I). These results further strengthen our model that SG formation functions to fluidize the cytoplasm and highlight a new potential function for ISRIB in the modulation of the physical properties of the cytoplasm.

Degradation of RNA by innate immune pathways increases mesoscale diffusivity in the cytoplasm

Our results are consistent with a model in which cytoplasmic RNAs restrict mesoscale particle motion and increase elastic confinement at the 100-nm length scale. This model predicts that decreasing the concentration of cytoplasmic RNA should increase mesoscale diffusivity. In mammalian cells, the antiviral RNase L[88,89] can be induced by transfecting cells with poly(I:C), leading to widespread cytosolic RNA degradation and formation of G3BP1 protein foci (Figure 6A).[90] We confirmed widespread reduction in cytosolic mRNA upon poly(I:C) treatment using poly(dT) FISH, and examined mesoscale scale diffusivity in cells with depleted mRNA (as indicated in live cells by formation of G3BP1 foci) (Figures 6B and 6C). These cells had G3BP1 tagged with GFP, necessitating use of GEMs in a different fluorescent channel. 40nm-GEMs were not bright enough when tagged with red-fluorescent proteins, therefore we developed a brighter GEM nanoparticle with a diameter of 50 nm (50nm-GEMs[91]) based on a *Quasibacillus thermotolerans* encapsulin scaffold[92] that enabled use of the red-fluorescent protein mScarlet. We confirmed that 50nm-GEMs were not sequestered within G3BP1-GFP foci (Figure S7E). Consistent with our hypothesis, we found that poly(I:C) treatment resulted in increased the diffusivity of 50nm-GEMs (Figure 6D; Figure S7F). These highlight the importance of RNA concentration as a determinant of the mesoscale physical properties of the cytoplasm in mammalian cells and show that an innate immune signaling pathway can change these properties.

Synthetic optogenetic condensation of RNA increases mesoscale diffusivity in the cytoplasm

To test whether RNA condensation can fluidize the mammalian cell cytoplasm independent of translation inhibition and polysome collapse, we developed a strategy to induce synthetic RNA condensates without cellular stress. Artificially assembled RNP granules containing the pumilio homology domain (PUM.HD) from the human Pumilio 1 protein were previously demonstrated to condense RNA.[93,94] We modified the artificial PUM.HD-RNP system by adding the homo-oligomerization cryptochrome 2 (CRY2) domain from *Arabidopsis thaliana*,[95,96] so that we could use blue light to control its dynamic assembly. We named this light-inducible condensate “opto-PUM” (Figure 6E). We also made a CRY2-mCherry construct with no RNA-binding domain, and named this “opto-control” (Figure 6E). Within minutes of blue light activation, we observed the formation of numerous opto-PUM foci, while no foci were formed in opto-control cells (Figure 6F). Addition of cycloheximide did not prevent opto-PUM foci formation upon blue light activation, suggesting that induction of opto-PUM foci does not require polysome collapse (Figure S7G). We then coexpressed 40nm-GEMs to quantify mesoscale diffusivity. 40nm-GEMs did not

Figure 5. Partitioning of mRNAs into SGs increases mesoscale particle diffusivity in mammalian cells

(A and B) Effective diffusivity at 100 ms ($D_{\text{eff-100ms}}$) for 40nm-GEMs upon sodium arsenite and heat stress. $N = 3$ biological replicates; $n > 50$ cells for all conditions. Boxes represent 5%–95% confidence intervals. Statistical comparisons by one-way ANOVA test; ns: not significant; $^{***}p < 0.001$.

(C) Schematic of predicted changes to polysomes and mRNA upon stress, with and without cycloheximide. Green: translation initiation complex; cyan: ribosomes; dark blue: mRNA; pink: SG; magenta: cycloheximide.

(D) Representative poly(dT) FISH images showing spatial distribution of mRNA in control and *G3BP 1/2 dKO* U2OS cells after 10-nM DMDA-PatA treatment for 30 min. Hoechst dye was used to stain DNA. Yellow arrows indicate mRNA foci. Scale bar: 10 μm.

(E and F) Change in effective diffusivities ($D_{\text{eff-100ms}}$) of 40nm-GEMs. The median $D_{\text{eff-100ms}}$ was measured for the same cell before and 30 min after each treatment. Each dot represents the fold change of median diffusivity of one cell; the $D_{\text{eff-100ms}}$ in the treatment condition (control = DMSO treatment) was normalized to the $D_{\text{eff-100ms}}$ for the same cell prior to treatment (0 min). $N = 3$ biological replicates; $n > 29$ cells for all conditions. Boxes represent 5%–95% confidence intervals. Statistical comparisons by one-way ANOVA test; ns: not significant; $^{*}p < 0.05$, $^{****}p < 0.0001$.

(G) Schematic of the effects of stresses on translation, and the mode of action of ISRIB.

(H and I) Effective diffusivity at 100 ms ($D_{\text{eff-100ms}}$) for 40nm-GEMs upon 200-nM ISRIB, 250 μM sodium arsenite ($NaAsO_2$), and 10 nM DMDA-PatA treatment for 30 min treatment. $N = 3$ biological replicates; $n > 50$ cells for all conditions. Boxes represent 5%–95% confidence intervals. Statistical comparisons by one-way ANOVA test; ns, not significant; $^{*}p < 0.05$, $^{**}p < 0.01$, $^{***}p < 0.001$, $^{****}p < 0.0001$.

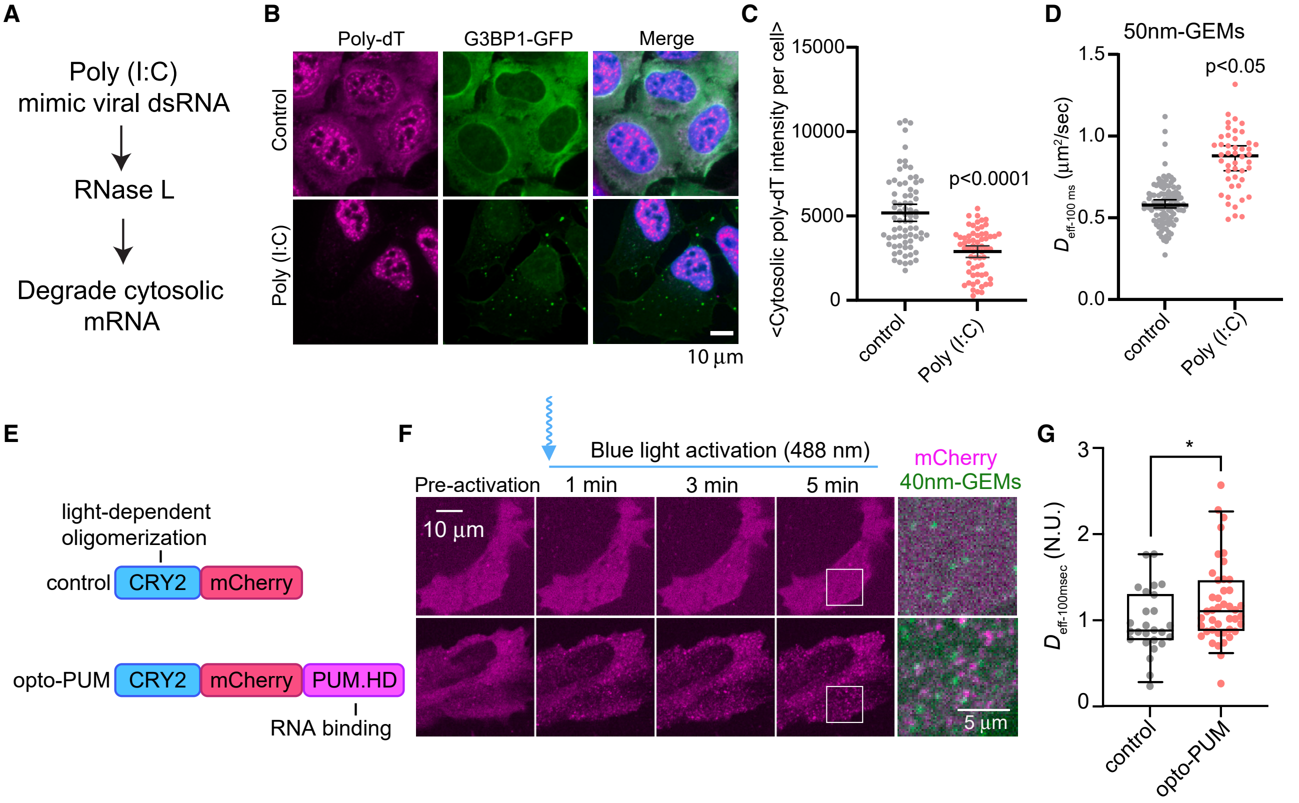

Figure 6. Degradation of RNA or artificially condensing RNA increases mesoscale diffusivity in the cytoplasm

(A) Mode of action of poly(I:C) induces cytosolic mRNAs degradation.

(B) Representative poly(dT) fluorescence *in situ* hybridization images of G3BP1-GFP, *G3BP1/2 dKO* U2OS cells, 2-h after transfection with 1 μg of poly(I:C) with 2 μL FuGENE 6 transfection reagent, control cells were transfected with FuGENE 6 transfection reagent only. Nuclei were stained by Hoechst, blue in the merged image. Scale bar: 10 μm.

(C) Quantification of average poly(dT) intensity in the cytosol (control: $n = 73$ cells; poly(I:C) treatment: $n = 63$ cells, statistical comparison was performed using a nonparametric Mann-Whitney test, median ± 5%–95% confidence interval).

(D) Effective diffusivity at 100 ms ($D_{\text{eff-100ms}}$) for 50nm-GEMs (control: $n = 103$ cells; poly(I:C) treatment: $n = 46$ cells, statistical comparison was performed using nonparametric Mann-Whitney test, median ± 5%–95% confidence interval).

(E) Graphic illustration of blue light-inducible opto-control and opto-PUM constructs.

(F) Representative live-cell images of U2OS cells expressing opto-Control or opto-PUM together with 40nm-GEMs, 488-nm blue light laser pulsed 100 ms at 25% laser power every 5 s for a period of 5 min to drive opto-PUM condensation.

(G) Fold change of median effective diffusivity ($D_{\text{eff-100ms}}$) for 40nm-GEMs in the indicated conditions. $D_{\text{eff-100ms}}$ after 30 min light exposure was normalized to the value in the same cell pretreatment. $N = 3$ biological replicates; $n = 26$ cells for opto-control, $n = 43$ for opto-PUM. Boxes represent 5%–95% confidence intervals. Statistical comparison was performed using a paired two-tailed t test. $^*p < 0.05$.

partition into opto-PUM foci, indicating that they are reliable probes of diffusivity (Figure 6F). We observed a significant increase in the diffusivity of 40nm-GEMs upon formation of opto-PUM foci (Figure 6G). These results are consistent with our model that RNA condensation can fluidize the cytoplasm.

DISCUSSION

Here, we found that polysome collapse and RNA condensation fluidize the cytoplasm. Polysome disassembly is necessary but not sufficient for cytoplasmic fluidization; rather, we found that mRNA condensation is also required to reduce elastic confinement and increase mesoscale diffusivity. Yeast mutants that fail to partition mRNAs into SGs show defects in mesoscale fluidization in several stresses, while mRNA condensation into P-bodies is most important in acute glucose starvation stress. We speculate that different mechanisms of mRNA condensation may be required because diverse stresses have distinct effects on other cytoplasmic physicochemical parameters, for example, cytosolic pH is most strongly decreased during glucose starvation.[2,3,46]

Estimates suggest that only 10% of cytoplasmic mRNAs partition into P-bodies and SGs during stress.[97–100] Thus, it may seem surprising that disruption of these condensates has such a pronounced effect on mesoscale diffusivity in the cell. We speculate that the concentration of mRNA and other polymers in the cytoplasm is close to a percolation transition, such that a small change in interaction propensity or concentration could lead to a significant change in physical properties[101,102]; an analogous percolation transition is the solidification that happens over a narrow temperature change when heating an egg.

Stresses that caused polysome collapse and SG formation also fluidized the cytoplasm in mammalian cells, and deletion of the key SG scaffolds G3BP1 and G3BP2 was sufficient to prevent this physical change. Furthermore, either degrading mRNA or partitioning mRNAs into synthetic condensates in the absence of stress both led to cytoplasmic fluidization. Thus, the phenomenon of mesoscale cytoplasmic fluidization driven by polysome collapse and RNA condensation into RNP granules is conserved over more than a billion years of eukaryotic evolution and likely of broad relevance.

It will be valuable to further characterize the biophysical effects of P-bodies in mammalian cells, or other types of cytosolic RNP granules such as the recently described TIS11B protein (also called *ZFP36L1*) granule (TIS granules), a large reticular meshwork that is intertwined with the endoplasmic reticulum (ER) driven by the RNA-binding protein TIS11B, which has been shown to compartmentalize some mRNAs near the ER.[103,104]

The dynamic biophysical changes that occur during stress are likely to have widespread impacts on biochemistry. We propose that the initial fluidization of the cytoplasm allows for rapid reorganization of the cell, enabling adaptation to the stress condition. In all stresses, proteins tend to misfold, and the creation of mesoscale membraneless organelles is an important mechanism to allow for refolding or degradation.[11] Phase separation of membraneless organelles requires mesoscale subassemblies to fuse together, a process that can be inhibited by mesoscale viscoelastic networks.[18,72] We found that the initial fluidization of the cytoplasm was important for the formation of Q-bodies. It will be interesting to investigate if other mesoscale assemblies that are known to assemble during ATP depletion, such as metabolic enzyme assemblies[3,37,105,106] also require cytoplasmic fluidization for their formation.

In addition to the formation of protein aggregates, changes in membrane structure have been observed during glucose starvation in yeast. Endocytosis and exocytosis change the complement of carbon transporters,[107] a process that requires efficient trafficking of vesicles of approximately 100 nm diameter. There are also large-scale changes in organelle structure, including mitochondrial morphology changes,[108] changes in inter-organelle connectivity, including mitochondria-ER contacts, and the nuclear-vacuole junction.[10] These findings indicate that membrane reorganization within the cytoplasm is critical to ensure cell survival during long-term stresses. Therefore, it will be interesting to investigate whether the fluidization of the cytoplasm also facilitates reorganization of membrane-bound organelles.

There is growing evidence for the involvement of SGs in human diseases. For example, cancer cells with oncogenic KRAS (Kirsten rat sarcoma viral oncogene homolog) mutations upregulate SGs through the production of bioactive lipid prostaglandins, leading to the inhibition of translation initiation factor eIF4A thereby increasing tumor fitness.[109] It will be interesting to test if the biophysical effects of SG assembly contribute to this adaptation.

Aberrant SG formation appears to be cytotoxic in neurodegenerative diseases.[110] The cytoplasmic pathology observed in end-stage neurodegeneration often involves the accumulation of unconventional SGs containing mislocalized RNA-binding proteins, such as aggregated FUS (Fused in Sarcoma)[111,112] or mutated TDP43 (transactive response DNA binding protein 43 kDa) with abnormal phosphorylation,[113] which is likely to alter the assembly kinetics of SGs and biophysical properties of the cytoplasm. Our study suggests that aberrant crowding and fluidity could contribute to the proteostatic collapse that is associated with all neurodegeneration. It is interesting to note that neurons typically have low levels of polysomes, and many mRNAs in neurites are translated as monosomes.[114] Furthermore, mRNA is typically transported in condensates or granules in neurons.[115,116] We speculate that these adaptations could help maintain fluidity and facilitate mesoscale motion in these complex cells.

Our findings provide key functional insights into the essential role of P-bodies and SGs. Furthermore, we reveal a unifying biophysical consequence of RNA condensation, establishing a new framework to investigate the role of RNA condensates in both normal physiology and disease.

Limitations of the study

We have not yet analyzed the importance of P-bodies in mammalian cells. We observed that P-bodies are constitutively induced in our cell lines possibly because they are cancer cells, or due to growth on stiff glass. It will be interesting to investigate primary cells and growth on softer substrates. We also do not have a reliable ~100-nm microrheology probe in mammalian cells and are currently developing new GEM nanoparticles to access this length scale. The difficulty in obtaining 3D data at high frame-rates prevented us from obtaining sufficiently long time-scale particle tracking to perfectly match our microrheology analysis to the timescales of Q-body formation. We were not able to visualize SGs in yeast cells. It has been shown that SGs are often diffraction-limited in yeast cells. Super-resolution imaging will be required to visualize these structures. Our simulation studies modeled RNA in a simplified way. Modeling RNA using detailed structural properties, including different contour lengths and surface charges will be interesting. Simulations also treat all polysomes as being of the same length, but future studies could instead explore a distribution of polysome lengths based on experimental quantifications.

STAR★METHODS

Detailed methods are provided in the online version of this paper and include the following:

- KEY RESOURCES TABLE
- RESOURCE AVAILABILITY
  - ○ Lead contact
  - ○ Materials availability
  - ○ Data and code availability
- EXPERIMENTAL MODEL AND STUDY PARTICIPANT DETAILS
  - ○ Yeast
  - ○ Human cell lines
- METHOD DETAILS
  - ○ Yeast strain construction
  - ○ Lentivirus production and cell transduction
  - ○ Transient transfection of mammalian cell lines

- ○ Yeast cell culture for imaging
  - ○ Drug treatments
  - ○ Sucrose gradient to fractionate polysomes
  - ○ Passive rheological probes imaging and single particle tracking
  - ○ Live yeast cell ATP sensor and pH sensor imaging and quantification
  - ○ Live yeast cell RNP granules and Q-bodies imaging and quantification
  - ○ Live yeast cell total cell volume, vacuole volume and cytosolic volume measurement
  - ○ Immunofluorescence
  - ○ Poly-dT FISH Imaging
  - ○ Blue-light activation of optogenetic artificial RNP condensates
  - ○ Cryo-electron tomography
  - ○ Coarse-grained molecular dynamic (MD) simulation
- ● QUANTIFICATION AND STATISTICAL ANALYSIS

SUPPLEMENTAL INFORMATION

Supplemental information can be found online at https://doi.org/10.1016/j.molcel.2024.06.024.

ACKNOWLEDGMENTS

We thank Sarah Keegan, Stephanie Patchett, Zoher Gueroui, Emily M. Sontag, Masakatsu Takaine, J. Paul Taylor, Daniel Romo, and Evgenia Zagoriy for reagents and technical assistance. We are grateful to all members of the Holt and Gresham labs, Saumya Saurabh, Nicholas Ingolia, and Roy Parker for feedback and advice. Figures 2C, 3A, 4E, and 5C and graphic illustration were created partly using Biorender. This work was supported by the NIH awards R01GM107466 (D.G.), R35GM153419 (D.G.), R35GM138312 (G.M.H.), R01GM132447 (L.J.H.), R37CA240765 (L.J.H.), and TR01 NS127186 (L.J.H.); the American Cancer Society Cornelia T Bailey Research Award (L.J.H.); the Hypothesis Fund (L.J.H.); the Air Force Office of Scientific Research FA9550-21-1-3503 0091 (L.J.H.); the Human Frontier Science Program RGP0016/2022-102 (L.J.H.); the European Research Council 3DCellPhase-760067 (J.M.); the Chan-Zuckerberg Initiative (J.M.); the EMBL (J.M.); the Simons Center for Computational Physical Chemistry at NYU (Simons Foundation 839534); and NYU IT High Performance Computing.

AUTHOR CONTRIBUTIONS

Y.X. designed and conducted experiments with help from T.L., and performed data analysis with T.S. G.M.H. undertook coarse-grained molecular dynamics simulations and analyzed data with T.S. M.-C.S. performed cryo-ET experiments, supervised by J.M. D.G. and L.J.H. supervised all aspects of the study. All authors contributed to writing and editing.

DECLARATION OF INTERESTS

The authors declare no competing interests.

Received: July 14, 2023
Revised: March 25, 2024
Accepted: June 24, 2024
Published: July 25, 2024

REFERENCES

1. Parry, B.R., Surovtsev, I.V., Cabeen, M.T., O'Hern, C.S., Dufresne, E.R., and Jacobs-Wagner, C. (2014). The bacterial cytoplasm has glass-like properties and is fluidized by metabolic activity. Cell *156*, 183–194. https://doi.org/10.1016/j.cell.2013.11.028.
2. Joyner, R.P., Tang, J.H., Helenius, J., Dultz, E., Brune, C., Holt, L.J., Huet, S., Müller, D.J., and Weis, K. (2016). A glucose-starvation response regulates the diffusion of macromolecules. Elife *5*, e09376. https://doi.org/10.7554/eLife.09376.
3. Munder, M.C., Midtvedt, D., Franzmann, T., Nüske, E., Otto, O., Herbig, M., Ulbricht, E., Müller, P., Taubenberger, A., Maharana, S., et al. (2016). A pH-driven transition of the cytoplasm from a fluid- to a solid-like state promotes entry into dormancy. Elife *5*, e09347. https://doi.org/10.7554/eLife.09347.
4. Görner, W., Durchschlag, E., Wolf, J., Brown, E.L., Ammerer, G., Ruis, H., and Schüller, C. (2002). Acute glucose starvation activates the nuclear localization signal of a stress-specific yeast transcription factor. EMBO J. *21*, 135–144. https://doi.org/10.1093/emboj/21.1.135.
5. Muzzey, D., Gómez-Uribe, C.A., Mettetal, J.T., and van Oudenaarden, A. (2009). A systems-level analysis of perfect adaptation in yeast osmoregulation. Cell *138*, 160–171. https://doi.org/10.1016/j.cell.2009.04.047.
6. Delaunay, A., Isnard, A.D., and Toledano, M.B. (2000). H2O2 sensing through oxidation of the Yap1 transcription factor. EMBO J. *19*, 5157–5166. https://doi.org/10.1093/emboj/19.19.5157.
7. Triandafillou, C.G., Katanski, C.D., Dinner, A.R., and Drummond, D.A. (2020). Transient intracellular acidification regulates the core transcriptional heat shock response. Elife *9*, e54880. https://doi.org/10.7554/eLife.54880.
8. Laidlaw, K.M.E., Bisinski, D.D., Shashkova, S., Paine, K.M., Veillon, M.A., Leake, M.C., and MacDonald, C. (2021). A glucose-starvation response governs endocytic trafficking and eisosomal retention of surface cargoes in budding yeast. J. Cell Sci. *134*, jcs257733. https://doi.org/10.1242/jcs.257733.
9. Seo, A.Y., Lau, P.-W., Feliciano, D., SenGupta, P., Gros, M.A.L., Cinquin, B., Larabell, C.A., and Lippincott-Schwartz, J. (2017). AMPK and vacuole-associated Atg14p orchestrate μ-lipophagy for energy production and long-term survival under glucose starvation. Elife *6*, e21690. https://doi.org/10.7554/eLife.21690.
10. Wood, N.E., Kositangool, P., Hariri, H., Marchand, A.J., and Henne, W.M. (2020). Nutrient Signaling, Stress Response, and Inter-organelle Communication Are Non-canonical Determinants of Cell Fate. Cell Rep. *33*, 108446. https://doi.org/10.1016/j.celrep.2020.108446.
11. Escusa-Toret, S., Vonk, W.I.M., and Frydman, J. (2013). Spatial sequestration of misfolded proteins by a dynamic chaperone pathway enhances cellular fitness during stress. Nat. Cell Biol. *15*, 1231–1243. https://doi.org/10.1038/ncb2838.
12. Kaganovich, D., Kopito, R., and Frydman, J. (2008). Misfolded proteins partition between two distinct quality control compartments. Nature *454*, 1088–1095. https://doi.org/10.1038/nature07195.
13. Sontag, E.M., Morales-Polanco, F., Chen, J.-H., McDermott, G., Dolan, P.T., Gestaut, D., Le Gros, M.A., Larabell, C., and Frydman, J. (2022). An ESCRT-dependent pathway coordinates Nuclear and Cytoplasmic Spatial Protein Quality Control at Nuclear vacuolar Junctions. Preprint at bioRxiv. https://doi.org/10.1101/2022.12.01.518779.
14. Sathyanarayanan, U., Musa, M., Bou Dib, P., Raimundo, N., Milosevic, I., and Krisko, A. (2020). ATP hydrolysis by yeast Hsp104 determines protein aggregate dissolution and size in vivo. Nat. Commun. *11*, 5226. https://doi.org/10.1038/s41467-020-19104-1.
15. Specht, S., Miller, S.B.M., Mogk, A., and Bukau, B. (2011). Hsp42 is required for sequestration of protein aggregates into deposition sites in Saccharomyces cerevisiae. J. Cell Biol. *195*, 617–629. https://doi.org/10.1083/jcb.201106037.
16. Ekman, A.A., Chen, J.-H., Guo, J., McDermott, G., Le Gros, M.A., and Larabell, C.A. (2017). Mesoscale imaging with cryo-light and X-rays: Larger than molecular machines, smaller than a cell. Biol. Cell *109*, 24–38. https://doi.org/10.1111/boc.201600044.
17. Holt, L.J., and Delarue, M. (2023). Macromolecular crowding: Sensing without a sensor. Curr. Opin. Cell Biol. *85*, 102269. https://doi.org/10.1016/j.ceb.2023.102269.
18. Shu, T., Mitra, G., Alberts, J., Viana, M.P., Levy, E.D., Hocky, G.M., and Holt, L.J. (2024). Mesoscale molecular assembly is favored by the active,

crowded cytoplasm. PRX Life *2*, 033001. https://doi.org/10.1103/PRXLife.2.033001.

19. Bonucci, M., Shu, T., and Holt, L.J. (2023). How it feels in a cell. Trends Cell Biol. *33*, 924–938. https://doi.org/10.1016/j.tcb.2023.05.002.
20. Carlini, L., Brittingham, G.P., Holt, L.J., and Kapoor, T.M. (2020). Microtubules Enhance Mesoscale Effective Diffusivity in the Crowded Metaphase Cytoplasm. Dev. Cell *54*, 574–582.e4. https://doi.org/10.1016/j.devcel.2020.07.020.
21. Delarue, M., Brittingham, G.P., Pfeffer, S., Surovtsev, I.V., Pinglay, S., Kennedy, K.J., Schaffer, M., Gutierrez, J.I., Sang, D., Poterewicz, G., et al. (2018). mTORC1 Controls Phase Separation and the Biophysical Properties of the Cytoplasm by Tuning Crowding. Cell *174*, 338–349.e20. https://doi.org/10.1016/j.cell.2018.05.042.
22. Advani, V.M., and Ivanov, P. (2019). Translational Control under Stress: Reshaping the Translatome. Bioessays *41*, e1900009. https://doi.org/10.1002/bies.201900009.
23. Crawford, R.A., and Pavitt, G.D. (2019). Translational regulation in response to stress in Saccharomyces cerevisiae. Yeast *36*, 5–21. https://doi.org/10.1002/yea.3349.
24. Janapala, Y., Preiss, T., and Shirokikh, N.E. (2019). Control of Translation at the Initiation Phase During Glucose Starvation in Yeast. Int. J. Mol. Sci. *20*, 4043. https://doi.org/10.3390/ijms20164043.
25. Ashe, M.P., De Long, S.K., and Sachs, A.B. (2000). Glucose depletion rapidly inhibits translation initiation in yeast. Mol. Biol. Cell *11*, 833–848. https://doi.org/10.1091/mbc.11.3.833.
26. Kuhn, K.M., DeRisi, J.L., Brown, P.O., and Sarnow, P. (2001). Global and specific translational regulation in the genomic response of Saccharomyces cerevisiae to a rapid transfer from a fermentable to a nonfermentable carbon source. Mol. Cell. Biol. *21*, 916–927. https://doi.org/10.1128/MCB.21.3.916-927.2001.
27. Bresson, S., Shchepachev, V., Spanos, C., Turowski, T.W., Rappsilber, J., and Tollervey, D. (2020). Stress-Induced Translation Inhibition through Rapid Displacement of Scanning Initiation Factors. Mol. Cell *80*, 470–484.e8. https://doi.org/10.1016/j.molcel.2020.09.021.
28. Decker, C.J., and Parker, R. (2012). P-bodies and stress granules: possible roles in the control of translation and mRNA degradation. Cold Spring Harb. Perspect. Biol. *4*, a012286. https://doi.org/10.1101/cshperspect.a012286.
29. Riggs, C.L., Kedersha, N., Ivanov, P., and Anderson, P. (2020). Mammalian stress granules and P bodies at a glance. J. Cell Sci. *133*, jcs242487. https://doi.org/10.1242/jcs.242487.
30. Rao, B.S., and Parker, R. (2017). Numerous interactions act redundantly to assemble a tunable size of P bodies in Saccharomyces cerevisiae. Proc. Natl. Acad. Sci. USA *114*, E9569–E9578. https://doi.org/10.1073/pnas.1712396114.
31. Jain, S., Wheeler, J.R., Walters, R.W., Agrawal, A., Barsic, A., and Parker, R. (2016). ATPase-Modulated Stress Granules Contain a Diverse Proteome and Substructure. Cell *164*, 487–498. https://doi.org/10.1016/j.cell.2015.12.038.
32. Glauninger, H., Bard, J.A.M., Wong Hickernell, C.J., Airoldi, E.M., Li, W., Singer, R.H., Paul, S., Fei, J., Sosnick, T.R., Wallace, E.W.J., et al. (2024). Transcriptome-wide mRNA condensation precedes stress granule formation and excludes stress-induced transcripts. Preprint at bioRxiv. https://doi.org/10.1101/2024.04.15.589678.
33. Desroches Altamirano, C., Kang, M.-K., Jordan, M.A., Borianne, T., Dilmen, I., Gnädig, M., von Appen, A., Honigmann, A., Franzmann, T.M., and Alberti, S. (2024). eIF4F is a thermo-sensing regulatory node in the translational heat shock response. Mol. Cell *84*, 1727–1741.e12. https://doi.org/10.1016/j.molcel.2024.02.038.
34. Glauninger, H., Wong Hickernell, C.J., Bard, J.A.M., and Drummond, D.A. (2022). Stressful steps: Progress and challenges in understanding stress-induced mRNA condensation and accumulation in stress granules. Mol. Cell *82*, 2544–2556. https://doi.org/10.1016/j.molcel.2022.05.014.
35. Mason, T.G., and Weitz, D.A. (1995). Optical measurements of frequency-dependent linear viscoelastic moduli of complex fluids. Phys. Rev. Lett. *74*, 1250–1253. https://doi.org/10.1103/PhysRevLett.74.1250.
36. Xiang, Y., Surovtsev, I.V., Chang, Y., Govers, S.K., Parry, B.R., Liu, J., and Jacobs-Wagner, C. (2021). Interconnecting solvent quality, transcription, and chromosome folding in Escherichia coli. Cell *184*, 3626–3642.e14. https://doi.org/10.1016/j.cell.2021.05.037.
37. Plante, S., Moon, K.-M., Lemieux, P., Foster, L.J., and Landry, C.R. (2023). Breaking spore dormancy in budding yeast transforms the cytoplasm and the solubility of the proteome. PLoS Biol. *21*, e3002042. https://doi.org/10.1371/journal.pbio.3002042.
38. Chambers, J.E., Zubkov, N., Kubánková, M., Nixon-Abell, J., Mela, I., Abreu, S., Schwiening, M., Lavarda, G., López-Duarte, I., Dickens, J.A., et al. (2022). Z-α1-antitrypsin polymers impose molecular filtration in the endoplasmic reticulum after undergoing phase transition to a solid state. Sci. Adv. *8*, eabm2094. https://doi.org/10.1126/sciadv.abm2094.
39. Shu, T., Szórádi, T., Kidiyoor, G.R., Xie, Y., Herzog, N.L., Bazley, A., Bonucci, M., Keegan, S., Saxena, S., Ettefa, F., et al. (2022). nucGEMs probe the biophysical properties of the nucleoplasm. Preprint at bioRxiv. https://doi.org/10.1101/2021.11.18.469159.
40. Heinrich, S., Sidler, C.L., Azzalin, C.M., and Weis, K. (2017). Stem-loop RNA labeling can affect nuclear and cytoplasmic mRNA processing. RNA *23*, 134–141. https://doi.org/10.1261/rna.057786.116.
41. Xie, Y., Gresham, D., and Holt, L. (2023). Increased mesoscale diffusivity in response to acute glucose starvation. Preprint at bioRxiv. https://doi.org/10.1101/2023.01.10.523352.
42. Einstein, A. (1905). Über die von der molekularkinetischen Theorie der Wärme geforderte Bewegung von in ruhenden Flüssigkeiten suspendierten Teilchen. Ann. Phys. *322*, 549–560. https://doi.org/10.1002/andp.19053220806.
43. Stokes, G.G. (1901). On the ffect of the Internal Friction of Fluids on the Motion of Pendulums. In Mathematical and Physical Papers (Cambridge University Press), pp. 1–10.
44. Weber, S.C., Thompson, M.A., Moerner, W.E., Spakowitz, A.J., and Theriot, J.A. (2012). Analytical tools to distinguish the effects of localization error, confinement, and medium elasticity on the velocity autocorrelation function. Biophys. J. *102*, 2443–2450. https://doi.org/10.1016/j.bpj.2012.03.062.
45. Martínez-Muñoz, G.A., and Kane, P. (2017). Vacuolar and plasma membrane proton pumps collaborate to achieve cytosolic pH homeostasis in yeast. J. Biol. Chem. *292*, 7743. https://doi.org/10.1074/jbc.A117.710470.
46. Gutierrez, J.I., Brittingham, G.P., Karadeniz, Y., Tran, K.D., Dutta, A., Holehouse, A.S., Peterson, C.L., and Holt, L.J. (2022). SWI/SNF senses carbon starvation with a pH-sensitive low-complexity sequence. Elife *11*, e70344. https://doi.org/10.7554/eLife.70344.
47. Yaginuma, H., Kawai, S., Tabata, K.V., Tomiyama, K., Kakizuka, A., Komatsuzaki, T., Noji, H., and Imamura, H. (2014). Diversity in ATP concentrations in a single bacterial cell population revealed by quantitative single-cell imaging. Sci. Rep. *4*, 6522. https://doi.org/10.1038/srep06522.
48. Takaine, M., Ueno, M., Kitamura, K., Imamura, H., and Yoshida, S. (2019). Reliable imaging of ATP in living budding and fission yeast. J. Cell Sci. *132*, jcs230649. https://doi.org/10.1242/jcs.230649.
49. Miesenböck, G., De Angelis, D.A., and Rothman, J.E. (1998). Visualizing secretion and synaptic transmission with pH-sensitive green fluorescent proteins. Nature *394*, 192–195. https://doi.org/10.1038/28190.
50. Boehlke, K.W., and Friesen, J.D. (1975). Cellular content of ribonucleic acid and protein in Saccharomyces cerevisiae as a function of exponential growth rate: calculation of the apparent peptide chain elongation rate.

J. Bacteriol. *121*, 429–433. https://doi.org/10.1128/jb.121.2.429-433.1975.

51. Waldron, C., Jund, R., and Lacroute, F. (1977). Evidence for a high proportion of inactive ribosomes in slow-growing yeast cells. Biochem. J. *168*, 409–415. https://doi.org/10.1042/bj1680409.
52. Miller, O.L., Jr., Hamkalo, B.A., and Thomas, C.A., Jr. (1970). Visualization of bacterial genes in action. Science *169*, 392–395. https://doi.org/10.1126/science.169.3943.392.
53. Arava, Y., Wang, Y., Storey, J.D., Liu, C.L., Brown, P.O., and Herschlag, D. (2003). Genome-wide analysis of mRNA translation profiles in Saccharomyces cerevisiae. Proc. Natl. Acad. Sci. USA *100*, 3889–3894. https://doi.org/10.1073/pnas.0635171100.
54. Ingolia, N.T., Ghaemmaghami, S., Newman, J.R.S., and Weissman, J.S. (2009). Genome-wide analysis in vivo of translation with nucleotide resolution using ribosome profiling. Science *324*, 218–223. https://doi.org/10.1126/science.1168978.
55. Ben-Shem, A., Garreau de Loubresse, N., Melnikov, S., Jenner, L., Yusupova, G., and Yusupov, M. (2011). The structure of the eukaryotic ribosome at 3.0 Å resolution. Science *334*, 1524–1529. https://doi.org/10.1126/science.1212642.
56. Balagopal, V., and Parker, R. (2011). Stm1 modulates translation after 80S formation in Saccharomyces cerevisiae. RNA *17*, 835–842. https://doi.org/10.1261/rna.2677311.
57. Schneider-Poetsch, T., Ju, J., Eyler, D.E., Dang, Y., Bhat, S., Merrick, W.C., Green, R., Shen, B., and Liu, J.O. (2010). Inhibition of eukaryotic translation elongation by cycloheximide and lactimidomycin. Nat. Chem. Biol. *6*, 209–217. https://doi.org/10.1038/nchembio.304.
58. Xue, L., Lenz, S., Zimmermann-Kogadeeva, M., Tegunov, D., Cramer, P., Bork, P., Rappsilber, J., and Mahamid, J. (2022). Publisher Correction: Visualizing translation dynamics at atomic detail inside a bacterial cell. Nature *611*, E13. https://doi.org/10.1038/s41586-022-05455-w.
59. de Teresa-Trueba, I., Goetz, S.K., Mattausch, A., Stojanovska, F., Zimmerli, C.E., Toro-Nahuelpan, M., Cheng, D.W.C., Tollervey, F., Pape, C., Beck, M., et al. (2023). Convolutional networks for supervised mining of molecular patterns within cellular context. Nat. Methods *20*, 284–294. https://doi.org/10.1038/s41592-022-01746-2.
60. Buchan, J.R., Muhlrad, D., and Parker, R. (2008). P bodies promote stress granule assembly in Saccharomyces cerevisiae. J. Cell Biol. *183*, 441–455. https://doi.org/10.1083/jcb.200807043.
61. Lui, J., Campbell, S.G., and Ashe, M.P. (2010). Inhibition of translation initiation following glucose depletion in yeast facilitates a rationalization of mRNA content. Biochem. Soc. Trans. *38*, 1131–1136. https://doi.org/10.1042/BST0381131.
62. Stoecklin, G., and Kedersha, N. (2013). Relationship of GW/P-bodies with stress granules. Adv. Exp. Med. Biol. *768*, 197–211. https://doi.org/10.1007/978-1-4614-5107-5_12.
63. Teixeira, D., Sheth, U., Valencia-Sanchez, M.A., Brengues, M., and Parker, R. (2005). Processing bodies require RNA for assembly and contain nontranslating mRNAs. RNA *11*, 371–382. https://doi.org/10.1261/rna.7258505.
64. Decker, C.J., Teixeira, D., and Parker, R. (2007). Edc3p and a glutamine/asparagine-rich domain of Lsm4p function in processing body assembly in Saccharomyces cerevisiae. J. Cell Biol. *179*, 437–449. https://doi.org/10.1083/jcb.200704147.
65. Xing, W., Muhlrad, D., Parker, R., and Rosen, M.K. (2020). A quantitative inventory of yeast P body proteins reveals principles of composition and specificity. Elife *9*, e56525. https://doi.org/10.7554/eLife.56525.
66. Currie, S.L., Xing, W., Muhlrad, D., Decker, C.J., Parker, R., and Rosen, M.K. (2023). Quantitative reconstitution of yeast RNA processing bodies. Proc. Natl. Acad. Sci. USA *120*, e2214064120. https://doi.org/10.1073/pnas.2214064120.
67. Riback, J.A., Katanski, C.A., Kear-Scott, J.L., Pilipenko, E.V., Sosnick, T.R., and Drummond, D.A. (2017). How evolution tunes stress-triggered protein phase separation to promote cell fitness during stress. Biophys. J. *112*, 5a. https://doi.org/10.1016/j.bpj.2016.11.047.
68. Holstege, F.C., Jennings, E.G., Wyrick, J.J., Lee, T.I., Hengartner, C.J., Green, M.R., Golub, T.R., Lander, E.S., and Young, R.A. (1998). Dissecting the regulatory circuitry of a eukaryotic genome. Cell *95*, 717–728. https://doi.org/10.1016/s0092-8674(00)81641-4.
69. Zenklusen, D., Larson, D.R., and Singer, R.H. (2008). Single-RNA counting reveals alternative modes of gene expression in yeast. Nat. Struct. Mol. Biol. *15*, 1263–1271. https://doi.org/10.1038/nsmb.1514.
70. Iserman, C., Desroches Altamirano, C., Jegers, C., Friedrich, U., Zarin, T., Fritsch, A.W., Mittasch, M., Domingues, A., Hersemann, L., Jahnel, M., et al. (2020). Condensation of Ded1p Promotes a Translational Switch from Housekeeping to Stress Protein Production. Cell *181*, 818–831.e19. https://doi.org/10.1016/j.cell.2020.04.009.
71. Kroschwald, S., Munder, M.C., Maharana, S., Franzmann, T.M., Richter, D., Ruer, M., Hyman, A.A., and Alberti, S. (2018). Different Material States of Pub1 Condensates Define Distinct Modes of Stress Adaptation and Recovery. Cell Rep. *23*, 3327–3339. https://doi.org/10.1016/j.celrep.2018.05.041.
72. Lee, D.S.W., Wingreen, N.S., and Brangwynne, C.P. (2021). Chromatin mechanics dictates subdiffusion and coarsening dynamics of embedded condensates. Nat. Phys. *17*, 531–538. https://doi.org/10.1038/s41567-020-01125-8.
73. Stein, K.C., and Frydman, J. (2019). The stop-and-go traffic regulating protein biogenesis: how translation kinetics controls proteostasis. J. Biol. Chem. *294*, 2076–2084. https://doi.org/10.1074/jbc.REV118.002814.
74. Takaine, M., Imamura, H., and Yoshida, S. (2022). High and stable ATP levels prevent aberrant intracellular protein aggregation in yeast. Elife *11*, e67659. https://doi.org/10.7554/eLife.67659.
75. Brewster, J.L., de Valoir, T., Dwyer, N.D., Winter, E., and Gustin, M.C. (1993). An osmosensing signal transduction pathway in yeast. Science *259*, 1760–1763. https://doi.org/10.1126/science.7681220.
76. Hohmann, S., Krantz, M., and Nordlander, B. (2007). Yeast osmoregulation. Methods Enzymol. *428*, 29–45. https://doi.org/10.1016/S0076-6879(07)28002-4.
77. Lavalée, M., Curdy, N., Laurent, C., Fournié, J.-J., and Franchini, D.-M. (2021). Cancer cell adaptability: turning ribonucleoprotein granules into targets. Trends Cancer *7*, 902–915. https://doi.org/10.1016/j.trecan.2021.05.006.
78. Ash, P.E.A., Vanderweyde, T.E., Youmans, K.L., Apicco, D.J., and Wolozin, B. (2014). Pathological stress granules in Alzheimer's disease. Brain Res. *1584*, 52–58. https://doi.org/10.1016/j.brainres.2014.05.052.
79. Yang, P., Mathieu, C., Kolaitis, R.-M., Zhang, P., Messing, J., Yurtsever, U., Yang, Z., Wu, J., Li, Y., Pan, Q., et al. (2020). G3BP1 Is a Tunable Switch that Triggers Phase Separation to Assemble Stress Granules. Cell *181*, 325–345.e28. https://doi.org/10.1016/j.cell.2020.03.046.
80. Guillén-Boixet, J., Kopach, A., Holehouse, A.S., Wittmann, S., Jahnel, M., Schlüßler, R., Kim, K., Trussina, I.R.E.A., Wang, J., Mateju, D., et al. (2020). RNA-Induced Conformational Switching and Clustering of G3BP Drive Stress Granule Assembly by Condensation. Cell *181*, 346–361.e17. https://doi.org/10.1016/j.cell.2020.03.049.
81. Broering, T.J. (2002). Initial Characterization of Reovirus Nonstructural Protein NS and Its Activities (University of Wisconsin–Madison).
82. Kudla, M., and Karginov, F.V. (2016). Measuring mRNA Translation by Polysome Profiling. Methods Mol. Biol. *1421*, 127–135. https://doi.org/10.1007/978-1-4939-3591-8_11.
83. Baliga, B.S., Cohen, S.A., and Munro, H.N. (1970). Effect of cycloheximide on the reaction of puromycin with polysome-bound peptidyl-tRNA. FEBS Lett. *8*, 249–252. https://doi.org/10.1016/0014-5793(70)80278-2.
84. Kommaraju, S.S., Aulicino, J., Gobbooru, S., Li, J., Zhu, M., Romo, D., and Low, W.-K. (2020). Investigation of the mechanism of action of a

potent pateamine A analog, des-methyl, des-amino pateamine A (DMDAPatA). Biochem. Cell Biol. *98*, 502–510. https://doi.org/10.1139/bcb-2019-0307.

85. Dang, Y., Kedersha, N., Low, W.-K., Romo, D., Gorospe, M., Kaufman, R., Anderson, P., and Liu, J.O. (2006). Eukaryotic initiation factor 2alpha-independent pathway of stress granule induction by the natural product pateamine A. J. Biol. Chem. *281*, 32870–32878. https://doi.org/10.1074/jbc.M606149200.

86. Anand, A.A., and Walter, P. (2020). Structural insights into ISRIB, a memory-enhancing inhibitor of the integrated stress response. FEBS Journal *287*, 239–245. https://doi.org/10.1111/febs.15073.

87. Sidrauski, C., McGeachy, A.M., Ingolia, N.T., and Walter, P. (2015). The small molecule ISRIB reverses the effects of eIF2α phosphorylation on translation and stress granule assembly. Elife *4*, e05033. https://doi.org/10.7554/eLife.05033.

88. Rath, S., Prangley, E., Donovan, J., Demarest, K., Wingreen, N.S., Meir, Y., and Korennykh, A. (2019). Concerted 2-5A-Mediated mRNA Decay and Transcription Reprogram Protein Synthesis in the dsRNA Response. Mol. Cell *75*, 1218–1228.e6. https://doi.org/10.1016/j.molcel.2019.07.027.

89. Burke, J.M., Moon, S.L., Matheny, T., and Parker, R. (2019). RNase L Reprograms Translation by Widespread mRNA Turnover Escaped by Antiviral mRNAs. Mol. Cell *75*, 1203–1217.e5. https://doi.org/10.1016/j.molcel.2019.07.029.

90. Decker, C.J., Burke, J.M., Mulvaney, P.K., and Parker, R. (2022). RNA is required for the integrity of multiple nuclear and cytoplasmic membraneless RNP granules. EMBO J. *41*, e110137. https://doi.org/10.15252/embj.2021110137.

91. Hernandez, C.M., Duran-Chaparro, D.C., van Eeuwen, T., Rout, M.P., and Holt, L.J. (2024). Development and Characterization of 50 Nanometer Diameter Genetically Encoded Multimeric Nanoparticles. Preprint at bioRxiv. https://doi.org/10.1101/2024.07.05.602291.

92. Giessen, T.W., Orlando, B.J., Verdegaal, A.A., Chambers, M.G., Gardener, J., Bell, D.C., Birrane, G., Liao, M., and Silver, P.A. (2019). Large protein organelles form a new iron sequestration system with high storage capacity. Elife *8*, e46070. https://doi.org/10.7554/eLife.46070.

93. Garcia-Jove Navarro, M., Kashida, S., Chouaib, R., Souquere, S., Pierron, G., Weil, D., and Gueroui, Z. (2019). RNA is a critical element for the sizing and the composition of phase-separated RNA–protein condensates. Nat. Commun. *10*, 3230. https://doi.org/10.1038/s41467-019-11241-6.

94. Cochard, A., Garcia-Jove Navarro, M., Piroska, L., Kashida, S., Kress, M., Weil, D., and Gueroui, Z. (2022). RNA at the surface of phase-separated condensates impacts their size and number. Biophys. J. *121*, 1675–1690. https://doi.org/10.1016/j.bpj.2022.03.032.

95. Che, D.L., Duan, L., Zhang, K., and Cui, B. (2015). The Dual Characteristics of Light-Induced Cryptochrome 2, Homo-oligomerization and Heterodimerization, for Optogenetic Manipulation in Mammalian Cells. ACS Synth. Biol. *4*, 1124–1135. https://doi.org/10.1021/acssynbio.5b00048.

96. Bugaj, L.J., Choksi, A.T., Mesuda, C.K., Kane, R.S., and Schaffer, D.V. (2013). Optogenetic protein clustering and signaling activation in mammalian cells. Nat. Methods *10*, 249–252. https://doi.org/10.1038/nmeth.2360.

97. Wang, C., Schmich, F., Srivatsa, S., Weidner, J., Beerenwinkel, N., and Spang, A. (2018). Correction: Context-dependent deposition and regulation of mRNAs in P-bodies. Elife *7*, e41300. https://doi.org/10.7554/eLife.41300.

98. Khong, A., Matheny, T., Jain, S., Mitchell, S.F., Wheeler, J.R., and Parker, R. (2017). The Stress Granule Transcriptome Reveals Principles of mRNA Accumulation in Stress Granules. Mol. Cell *68*, 808–820.e5. https://doi.org/10.1016/j.molcel.2017.10.015.

99. Namkoong, S., Ho, A., Woo, Y.M., Kwak, H., and Lee, J.H. (2018). Systematic Characterization of Stress-Induced RNA Granulation. Mol. Cell *70*, 175–187.e8. https://doi.org/10.1016/j.molcel.2018.02.025.

100. Matheny, T., Rao, B.S., and Parker, R. (2019). Transcriptome-Wide Comparison of Stress Granules and P-Bodies Reveals that Translation Plays a Major Role in RNA Partitioning. Mol. Cell. Biol. *39*, e00313-19. https://doi.org/10.1128/MCB.00313-19.

101. Kar, M., Dar, F., Welsh, T.J., Vogel, L.T., Kühnemuth, R., Majumdar, A., Krainer, G., Franzmann, T.M., Alberti, S., Seidel, C.A.M., et al. (2022). Phase-separating RNA-binding proteins form heterogeneous distributions of clusters in subsaturated solutions. Proc. Natl. Acad. Sci. USA *119*, e2202222119. https://doi.org/10.1073/pnas.2202222119.

102. Mittag, T., and Pappu, R.V. (2022). A conceptual framework for understanding phase separation and addressing open questions and challenges. Mol. Cell *82*, 2201–2214. https://doi.org/10.1016/j.molcel.2022.05.018.

103. Ma, W., and Mayr, C. (2018). A Membraneless Organelle Associated with the Endoplasmic Reticulum Enables 3’UTR-Mediated Protein-Protein Interactions. Cell *175*, 1492–1506.e19. https://doi.org/10.1016/j.cell.2018.10.007.

104. Horste, E.L., Fansler, M.M., Cai, T., Chen, X., Mitschka, S., Zhen, G., Lee, F.C.Y., Ule, J., and Mayr, C. (2023). Subcytoplasmic location of translation controls protein output. Mol. Cell *83*, 4509–4523.e11. https://doi.org/10.1016/j.molcel.2023.11.025.

105. Marini, G., Nüske, E., Leng, W., Alberti, S., and Pigino, G. (2020). Reorganization of budding yeast cytoplasm upon energy depletion. Mol. Biol. Cell *31*, 1232–1245. https://doi.org/10.1091/mbc.E20-02-0125.

106. Petrovska, I., Nüske, E., Munder, M.C., Kulasegaran, G., Malinovska, L., Kroschwald, S., Richter, D., Fahmy, K., Gibson, K., Verbavatz, J.-M., et al. (2014). Filament formation by metabolic enzymes is a specific adaptation to an advanced state of cellular starvation. Elife *3*, e02409. https://doi.org/10.7554/eLife.02409.

107. Feyder, S., De Craene, J.-O., Bär, S., Bertazzi, D.L., and Friant, S. (2015). Membrane trafficking in the yeast Saccharomyces cerevisiae model. Int. J. Mol. Sci. *16*, 1509–1525. https://doi.org/10.3390/ijms16011509.

108. Laporte, D., Gouleme, L., Jimenez, L., Khemiri, I., and Sagot, I. (2018). Mitochondria reorganization upon proliferation arrest predicts individual yeast cell fate. Elife *7*, e35685. https://doi.org/10.7554/eLife.35685.

109. Grabocka, E., and Bar-Sagi, D. (2016). Mutant KRAS Enhances Tumor Cell Fitness by Upregulating Stress Granules. Cell *167*, 1803–1813.e12. https://doi.org/10.1016/j.cell.2016.11.035.

110. Zhang, P., Fan, B., Yang, P., Temirov, J., Messing, J., Kim, H.J., and Taylor, J.P. (2019). Chronic optogenetic induction of stress granules is cytotoxic and reveals the evolution of ALS-FTD pathology. Elife *8*, e39578. https://doi.org/10.7554/eLife.39578.

111. Dormann, D., Rodde, R., Edbauer, D., Bentmann, E., Fischer, I., Hruscha, A., Than, M.E., Mackenzie, I.R.A., Capell, A., Schmid, B., et al. (2010). ALS-associated fused in sarcoma (FUS) mutations disrupt Transportin-mediated nuclear import. EMBO J. *29*, 2841–2857. https://doi.org/10.1038/emboj.2010.143.

112. Deng, H., Gao, K., and Jankovic, J. (2014). The role of FUS gene variants in neurodegenerative diseases. Nat. Rev. Neurol. *10*, 337–348. https://doi.org/10.1038/nrneurol.2014.78.

113. Neumann, M., Kwong, L.K., Lee, E.B., Kremmer, E., Flatley, A., Xu, Y., Forman, M.S., Troost, D., Kretzschmar, H.A., Trojanowski, J.Q., et al. (2009). Phosphorylation of S409/410 of TDP-43 is a consistent feature in all sporadic and familial forms of TDP-43 proteinopathies. Acta Neuropathol. *117*, 137–149. https://doi.org/10.1007/s00401-008-0477-9.

114. Biever, A., Glock, C., Tushev, G., Ciirdaeva, E., Dalmay, T., Langer, J.D., and Schuman, E.M. (2020). Monosomes actively translate synaptic

mRNAs in neuronal processes. Science *367*. https://doi.org/10.1126/science.aay4991.

115. Knowles, R.B., Sabry, J.H., Martone, M.E., Deerinck, T.J., Ellisman, M.H., Bassell, G.J., and Kosik, K.S. (1996). Translocation of RNA granules in living neurons. J. Neurosci. *16*, 7812–7820. https://doi.org/10.1523/JNEUROSCI.16-24-07812.1996.
116. Liao, Y.-C., Fernandopulle, M.S., Wang, G., Choi, H., Hao, L., Drerup, C.M., Patel, R., Qamar, S., Nixon-Abell, J., Shen, Y., et al. (2019). RNA Granules Hitchhike on Lysosomes for Long-Distance Transport, Using Annexin A11 as a Molecular Tether. Cell *179*, 147–164.e20. https://doi.org/10.1016/j.cell.2019.08.050.
117. Bharat, T.A.M., and Scheres, S.H.W. (2016). Resolving macromolecular structures from electron cryo-tomography data using subtomogram averaging in RELION. Nat. Protoc. *11*, 2054–2065. https://doi.org/10.1038/nprot.2016.124.
118. Botman, D., de Groot, D.H., Schmidt, P., Goedhart, J., and Teusink, B. (2019). In vivo characterisation of fluorescent proteins in budding yeast. Sci. Rep. *9*, 2234. https://doi.org/10.1038/s41598-019-38913-z.
119. Hentges, P., Van Driessche, B., Tafforeau, L., Vandenhaute, J., and Carr, A.M. (2005). Three novel antibiotic marker cassettes for gene disruption and marker switching in Schizosaccharomyces pombe. Yeast *22*, 1013–1019. https://doi.org/10.1002/yea.1291.
120. Anderson, J.A., Glaser, J., and Glotzer, S.C. (2020). HOOMD-blue: A Python package for high-performance molecular dynamics and hard particle Monte Carlo simulations. Comput. Mater. Sci. *173*, 109363. https://doi.org/10.1016/j.commatsci.2019.109363.
121. Mastronarde, D.N. (2005). Automated electron microscope tomography using robust prediction of specimen movements. J. Struct. Biol. *152*, 36–51. https://doi.org/10.1016/j.jsb.2005.07.007.
122. Kremer, J.R., Mastronarde, D.N., and McIntosh, J.R. (1996). Computer visualization of three-dimensional image data using IMOD. J. Struct. Biol. *116*, 71–76.
123. Tegunov, D., and Cramer, P. (2019). Real-time cryo-electron microscopy data preprocessing with Warp. Nat. Methods *16*, 1146–1152. https://doi.org/10.1038/s41592-019-0580-y.
124. Tegunov, D., Xue, L., Dienemann, C., Cramer, P., and Mahamid, J. (2021). Multi-particle cryo-EM refinement with M visualizes ribosome-antibiotic complex at 3.5 Å in cells. Nat. Methods *18*, 186–193. https://doi.org/10.1038/s41592-020-01054-7.
125. Kimanius, D., Dong, L., Sharov, G., Nakane, T., and Scheres, S.H.W. (2021). New tools for automated cryo-EM single-particle analysis in RELION-4.0. Biochem. J. *478*, 4169–4185. https://doi.org/10.1042/BCJ20210708.
126. Pettersen, E.F., Goddard, T.D., Huang, C.C., Meng, E.C., Couch, G.S., Croll, T.I., Morris, J.H., and Ferrin, T.E. (2021). UCSF ChimeraX: Structure visualization for researchers, educators, and developers. Protein Sci. *30*, 70–82. https://doi.org/10.1002/pro.3943.
127. Tang, G., Peng, L., Baldwin, P.R., Mann, D.S., Jiang, W., Rees, I., and Ludtke, S.J. (2007). EMAN2: an extensible image processing suite for electron microscopy. J. Struct. Biol. *157*, 38–46. https://doi.org/10.1016/j.jsb.2006.05.009.
128. Klumpe, S., Fung, H.K., Goetz, S.K., Zagoriy, I., Hampoelz, B., Zhang, X., Erdmann, P.S., Baumbach, J., Müller, C.W., Beck, M., et al. (2021). A modular platform for automated cryo-FIB workflows. Elife *10*, e70506. https://doi.org/10.7554/eLife.70506.
129. Riback, J.A., Katanski, C.D., Kear-Scott, J.L., Pilipenko, E.V., Rojek, A.E., Sosnick, T.R., and Drummond, D.A. (2017). Stress-Triggered Phase Separation Is an Adaptive, Evolutionarily Tuned Response. Cell *168*, 1028–1040.e19. https://doi.org/10.1016/j.cell.2017.02.027.
130. Sbalzarini, I.F., and Koumoutsakos, P. (2005). Feature point tracking and trajectory analysis for video imaging in cell biology. J. Struct. Biol. *151*, 182–195. https://doi.org/10.1016/j.jsb.2005.06.002.
131. Takaine, M. (2019). QUEEN-based Spatiotemporal ATP Imaging in Budding and Fission Yeast. Bio Protoc. *9*, e3320. https://doi.org/10.21769/BioProtoc.3320.
132. Chan, Y.-H.M., and Marshall, W.F. (2014). Organelle size scaling of the budding yeast vacuole is tuned by membrane trafficking rates. Biophys. J. *106*, 1986–1996. https://doi.org/10.1016/j.bpj.2014.03.014.
133. Villa, E., Schaffer, M., Plitzko, J.M., and Baumeister, W. (2013). Opening windows into the cell: focused-ion-beam milling for cryo-electron tomography. Curr. Opin. Struct. Biol. *23*, 771–777. https://doi.org/10.1016/j.sbi.2013.08.006.
134. Schaffer, M., Engel, B.D., Laugks, T., Mahamid, J., Plitzko, J.M., and Baumeister, W. (2015). Cryo-focused Ion Beam Sample Preparation for Imaging Vitreous Cells by Cryo-electron Tomography. Bio Protoc. *5*, 5. https://doi.org/10.21769/bioprotoc.1575.
135. Schaffer, M., Mahamid, J., Engel, B.D., Laugks, T., Baumeister, W., and Plitzko, J.M. (2017). Optimized cryo-focused ion beam sample preparation aimed at in situ structural studies of membrane proteins. J. Struct. Biol. *197*, 73–82. https://doi.org/10.1016/j.jsb.2016.07.010.
136. Hagen, W.J.H., Wan, W., and Briggs, J.A.G. (2017). Implementation of a cryo-electron tomography tilt-scheme optimized for high resolution subtomogram averaging. J. Struct. Biol. *197*, 191–198. https://doi.org/10.1016/j.jsb.2016.06.007.
137. Zheng, S., Wolff, G., Greenan, G., Chen, Z., Faas, F.G.A., Bárcena, M., Koster, A.J., Cheng, Y., and Agard, D.A. (2022). AreTomo: an integrated software package for automated marker-free, motion-corrected cryo-electron tomographic alignment and reconstruction. J. Struct. Biol. X *6*, 100068. https://doi.org/10.1016/j.yjsbx.2022.100068.
138. Weeks, J.D., Chandler, D., and Andersen, H.C. (1971). Role of repulsive forces in determining the equilibrium structure of simple liquids. J. Chem. Phys. *54*, 5237–5247. https://doi.org/10.1063/1.1674820.
139. Frenkel, D., and Smit, B. (2023). Understanding Molecular Simulation: From Algorithms to Applications (Elsevier).
140. Stukowski, A. (2009). Visualization and analysis of atomistic simulation data with OVITO–the Open Visualization Tool. Modell. Simul. Mater. Sci. Eng. *18*, 015012.
141. Keegan, S., Fenyö, D., and Holt, L.J. (2023). GEMspa: a Napari plugin for analysis of single particle tracking data. Preprint at bioRxiv. https://doi.org/10.1101/2023.06.26.546612.

STAR★METHODS

KEY RESOURCES TABLE

REAGENT or RESOURCE	SOURCE	IDENTIFIER
Antibodies		
Mouse monoclonal Anti-G3BP1	Santa Cruz	Cat#sc-81940, RRID: AB_1123055
Goat anti-Mouse IgG (H+L) Highly Cross-Adsorbed Secondary Antibody, Alexa Fluor 647	Thermo Fisher Scientific	Cat#A21236, RRID: AB_2535805
Bacterial and virus strains		
One Shot Stbl3 Chemically Competent E. coli	Thermo Fisher Scientific	Cat#C737303
Chemicals, peptides, and recombinant proteins		
2-Deoxy-D-glucose	Sigma-Alrich	Cat#D8375
Antimycin A	Sigma-Alrich	Cat#A8674
Concanavalin A	Sigma-Alrich	Cat#11028-71-0
Cycloheximide	Sigma-Alrich	Cat#C7698
Puromycin	MedChem Express	Cat#HY-B1743A
ISRIB	Sigma-Alrich	Cat#SML0843
Des-methyl, des-amino pateamine A (DMDA PatA)	Daniel Romo lab	N/A
Hoechst 33342 solution	Thermo Fisher Scientific	Cat#62249
Poly (I:C) HMW	InvivoGen	Cat#31852-29-6
Oligo $(dT)_{30}$-Alexa647	IDT	N/A
HCR RNA-FISH Probe hybridization Buffers	Molecular Instruments	N/A
HCR RNA-FISH Probe Wash Buffers	Molecular Instruments	N/A
Critical commercial assays		
Q5 High-Fidelity 2X Master Mix	NEB	Cat#M0492S
FuGENE HD reagent	Promega	Cat#E5912
Deposited data		
The *S. cerevisiae* 80S ribosome map	Electron Microscopy Data Bank (EMDB)	EMD: 3228[117]
Subtomogram average of 80S ribosomes in native *S. cerevisiae*	This paper	EMD: 50409
Subtomogram average of 80S ribosomes in *S. cerevisiae* under acute glucose starvation	This paper	EMD: 50415
Tilt series (TS) frames (+ detector count reference file)	This paper	EMPIAR: 12104
Tilt eries metadata files (original mdocs, mdocs with bad tilts removed; xf files, rawtlt and st files created by Warp)	This paper	EMPIAR: 12104
Tomograms	This paper	EMPIAR: 12104
Segmentations	This paper	EMPIAR: 12104
Particle coordinates	This paper	EMPIAR: 12104
Starfiles with translations and orientations of subtomograms	This paper	EMPIAR: 12104
Experimental models: Cell lines		
HEK293T human cell line	This paper	N/A
U2OS human cell line	J. Paul Taylor lab	N/A
U2OS *G3BP1/2 dKO* human cell line	J. Paul Taylor lab	N/A
U2OS *G3BP1/2 dKO* G3BP1-GFP human cell line	J. Paul Taylor lab	N/A
U2OS pUBC-40nm-GEMs-Sapphire human cell line	This paper	N/A
U2OS *G3BP1/2 dKO* pUBC-40nm-GEMs-Sapphire human cell line	This paper	N/A

(*Continued on next page*)

Continued

REAGENT or RESOURCE	SOURCE	IDENTIFIER
U2OS *G3BP1/2 dKO* G3BP1-GFP pUBC-50nm-GEMs-mScarlet human cell line	This paper	N/A
Experimental models: Organisms/strains		
BY4741 *MATa his21 leu20 met150 ura30* pINO4::pINO4-40nm-GEMs-Sapphire-LEU2	This paper	LH4248
MATa his21 leu20 met150 ura30 Ura3::pHis3-GFP-μNS	This paper	LH4544
BY4741 *MATa his21 leu20 met150 ura30* His3::pTEF -QUEEN-2m-tCYC1	This paper	LH4819
BY4741 *MATa his21 leu20 met150 ura30* Leu2::pTDH3-pHluorin-tTDH3	This paper	LH4820
BY4741 *MATa his21 leu20 met150 ura30* Leu2:: pTDH3-pHluorin-tTDH3	This paper	LH4820
BY4741 *MATa his21 leu20 met150 ura30* Dcp2-mScarlet::HIS3, Pab1-mNeoGreen::NatNT	This paper	LH4821
BY4741 *MATalpha his21 leu20 met150 ura30* Dcp2-mScarlet::HIS3, Pab1-mNeoGreen::NatNT, *edc3Δ::hphMX*	This paper	LH4822
BY4741 *MATa his21 leu20 met150 ura30* Ura3::pHIS3-GFP-μNS, Dcp2-mScarlet::HIS3	This paper	LH4823
BY4741 *MATa his21 leu20 met150 ura30* pINO4::pINO4-40nm-GEMs-Sapphire-LEU2, Dcp2-mScarlet::HIS3	This paper	LH4824
BY4741 *MATalpha his21 leu20 met150 ura30* *edc3Δ::hphMX*, Ura3::pHIS3-GFP-μNS	This paper	LH4560
W303 *MATa pab1ΔP*, Ura3::pHIS3-GFP-μNS	This paper	LH4863
BY4741 *MATa his21 leu20 met150 ura30 edc3Δ::NatRMX,* pINO4::pINO4-Pfv-Sapphire::LEU2	This paper	LH4825
BY4741 *MATalpha his21 leu20 met150 ura30* Hsp42-mScarlet::HIS3	This paper	LH4565
BY4741 *MATalpha his21 leu20 met150 ura30* *edc3Δ::hphMX*, Hsp42-mScarlet::HIS3	This paper	LH4566
BY4741 *MATalpha his21 leu20 met150 ura30* Vph1-TdTomato::KanMX, His3::pGPD-NeoGreen-PLCΔ-PH2	This paper	LH4406
BY4741 *MATa his21 leu20 met150 ura30* Ura3::pHIS3-GFP-μNS, Hsp42-mScarlet::HIS3	This paper	LH4875
Recombinant DNA		
Yeast plasmid pRS305-Leu2-pINO4-40nm-GEMs-Sapphire	Addgene # 116930	pLH497
Yeast plasmid pRS306-pHIS3-GFP-μNS	Addgene # 116935	pLH1125
Yeast plasmid pFA6a-ymScarletI-SpHIS5	Botman et al.[118]	pLH1688
Yeast plasmid pFA6a-mNeonGreen-natNT2	Addgene plasmid # 129099	pLH1532
Yeast plasmid pFA6a-hphMX6	Hentges et al.[119]	pLH1493
Yeast plasmid pFA6a-natMX6	Hentges et al.[119]	pLH1494
Yeast plasmid pTEF1-QUEEN-2m-tCYC1	Masakatsu Takaine lab	pLH2156
Yeast plasmid pRS305-pTDH3-pHluorin-tTDH3	Gutierrez et al.[46]	pLH1097
Mammalian plasmid pUBC-40nm-GEMs-Sapphire	Shu et al.[39]	pLH1984
Mammalian plasmid pUBC-50nm-GEMs-mScarlet	This paper	pLH2328
Mammalian plasmid pMD2.G	Addgene #12259	pLH1863
Mammalian plasmid psPAX2	Addgene #12260	pLH1864
Mammalian plasmid pHR-mCherry-Cry2WT	Addgene #101221	pLH1972
Mammalian plasmid pHR-PUM.HD-mCherry-Cry2WT	This paper	pLH2126

(*Continued on next page*)

Continued

REAGENT or RESOURCE	SOURCE	IDENTIFIER
Software and algorithms		
NIS Elements	Nikon	https://www.microscope.healthcare.nikon.com/products/software/nis-elements/viewer
Fiji	Open source	https://imagej.net/software/fiji/
Prism 10	GraphPad Software	https://www.graphpad.com/
Python	Open source	https://www.python.org/downloads/release/python-370/
MATLAB	MathWorks	https://www.mathworks.com/
HOOMD-Blue, v3.7.0	Anderson et al.[120]	https://glotzerlab.engin.umich.edu/hoomd-blue/
SerialEM	Mastronarde[121]	https://bio3d.colorado.edu/SerialEM/
IMOD package	Kremer et al.[122]	https://bio3d.colorado.edu/imod/
Warp 1.0.9	Tegunov and Cramer[123]	http://www.warpem.com/
M 1.0.9	Tegunov et al.[124]	http://www.warpem.com/
RELION 4.0.1	Kimanius et al.[125]	https://relion.readthedocs.io/en/release-4.0/
ChimeraX 1.1.1	Pettersen et al.[126]	https://www.cgl.ucsf.edu/chimerax/
EMAN2	Tang et al.[127]	https://blake.bcm.edu/emanwiki/EMAN2
MAPS 3	ThermoFisher Scientific	https://www.thermofisher.com/de/de/home/electron-microscopy/products/software-em-3d-vis/maps-software.html
DeePiCt	de Teresa-Trueba et al.[59]	https://github.com/irenedet/3d-unet/tree/7bc343971bdb818c5de90570b83731c8d77cde04
SerialFIB	Klumpe et al.[128]	https://github.com/sklumpe/SerialFIB

RESOURCE AVAILABILITY

Lead contact

Further information and requests for resources and reagents should be directed to and will be fulfilled by the lead contact, Liam J. Holt (Liam.Holt@nyulangone.org).

Materials availability

Plasmids generated in this study have been deposited to Addgene.

All materials will be made available on request.

Data and code availability

- The *S. cerevisiae* 80S ribosome map used as reference for subtomogram analysis was obtained from the Electron Microscopy Data Bank (EMDB) under accession code EMD: 3228.[117] Tomograms generated and analyzed in this study are deposited in the Electron Microscopy Public Image Archive under accession code EMPIAR: 12104. Subtomogram averages of ribosomes from cells in control and starvation conditions are deposited in the EMDB under accession codes EMD: 50409 and EMD: 50415, respectively.
- All original code has been deposited at Zenodo (https://zenodo.org/records/11223623), original imaging data have been deposited at Mendeley Data (https://data.mendeley.com/datasets/v39bywm9z6/1) and are publicly available as of the date of publication.
- Any additional information required to reanalyze the data reported in this paper is available from the lead contact upon request.

EXPERIMENTAL MODEL AND STUDY PARTICIPANT DETAILS

Yeast

Saccharomyces cerevisiae BY4741 and W303 strains were grown in synthetic complete media + 2% dextrose (SCD) according to standard Cold Spring Harbor Protocols unless otherwise stated. Exponentially growing cultures between OD_{600} 0.1 and 0.4 were used in all experiments unless otherwise noted.

Human cell lines

U2OS cells (Kindly provided by J. Paul Taylor lab) were cultured in DMEM containing high glucose and sodium pyruvate supplemented with 10%FBS and 50 U/mL penicillin, and 50 μg/mL streptomycin (Gibco, Cat. No. 15140122), and maintained at 37°C in a humidified incubator with 5% CO_2. Cells were regularly split in fresh medium upon reaching 80%-90% confluency. All cells were routinely tested for mycoplasma by PCR screening of the conditioned medium.

METHOD DETAILS

Yeast strain construction

Endogenous protein tagging at the C terminal with fluorescent protein was constructed via transformation of PCR products containing fluorescent proteins with auxotrophic marker gene, using either plasmid pLH1688 or pLH1532.[118] The PCR products contained 42 bp of homology to the 5′ and 3′ of the target gene stop codon region. Deletion strains were constructed via transformation with PCR products containing antibiotic resistance cassettes (pLH1493 and pLH1494).[119] PCR products contained 42bp of homology to the 5′ and 3′ genomic regions immediately adjacent to the gene to be deleted. The scarless Pab1 P-domain (419–502 amino acid) deletion strain was generated following the protocol outlined in Riback et al.[129] Briefly, WT W303 yeast cells were first transformed with a URA3 expression cassette replacing the Pab1 P-domain, which contained flanking DNA and included a stop codon at the beginning of the cassette. The resulting intermediate strain was selected on SCD-Ura plates and confirmed through colony PCR and sequencing. Subsequently, this intermediate strain was transformed with a synthesized dsDNA containing only genes upstream and downstream of P-domain, excluding the P-domain itself. Transformants were selected on plates containing 5-FOA. Single colonies of scarless Pab1 P-domain deletion were isolated and verified using colony PCR and sequencing. To integrate either 40nm-GEMs or μNS particles into the yeast strain, plasmid pLH497 was linearized by restriction enzyme SnaBI, and pLH1125 was linearized by primers located at the HIS3 promoter region. To integrate the ATP sensor QUEEN or pH sensor pHluorin, plasmid pLH2156 (a gift from Satoshi Yoshida lab) was linearized by restriction enzyme PstI, plasmid pLH1097 was linearized by restriction enzyme KasI. All DNA products were transformed to the yeast strains based on lithium acetate approach according to standard protocol.

Lentivirus production and cell transduction

HEK293T cells (9×10^6 per 15 cm dish) were plated in antibiotic free DMEM (Gibco, Cat. No. 11995073) supplemented with 10%FBS (Gemini bio-products, Cat. no. 100-106). The next day, cells were transfected with transgene plasmid (pLH1984) together with lentivirus packaging plasmids psPAX2 and pMD2.G, using fuGENE HD transfection reagent (Promega, Cat. no. E2312) following manufacturer's protocol. 24 h later, 15 mL antibiotic free DMEM was replaced and the supernatants were collected at both 48 and 72 h post-transfection, and stored at 4°C. Virus titers were concentrated by centrifugation at 4,000 rcf for 40 min in an Amicon Ultra-15 30 KDa centrifugal filter (MilliporeSigma, Cat. No. UFC903024). Concentrated viral suspensions were aliquoted and stored at −80°C until later use. Lentivirus was introduced into U2OS wild type and *G3BP1/2 dKO* cell lines of interest via reverse transduction with 1-10 μL of concentrated virus in fresh media, and replacing media after 24 h. After cell lines stabilized, they were frozen in 10% DMSO (Sigma-Aldrich, Cat. no. D2650- 100) in FBS (Gemini bio-products, Cat. no. 100-106) and thawed for use in experiments whenever needed.

Transient transfection of mammalian cell lines

For transfection, U2OS cells were seeded as 60%–70% confluency in a 6-well glass bottom plate (Cellvis, Cat. No. P06-1.5H-N) on the day before transfection and were transfected with 1 μg of plasmid DNA (pLH1972 or pLH2126) or Poly (I:C) (long synthetic analog of dsRNA, InvivoGen) per well using FuGENE HD reagent per manufacturer guidelines. 24 h post-transfection, fresh DMEM medium was replaced. And imaging experiments were usually carried out between 24 and 48 h post-transfection.

Yeast cell culture for imaging

Saccharomyces cerevisiae strains were revived from a −80°C freezer on YPD plate for overnight growth. The next day, a patch of yeast cells were inoculated into 5-mL synthetic complete media with 2% glucose (SCD), and the cultures were grown at 30°C in a rotating incubator for 5-6 h without exceeding an OD_{600} of 0.4. Afterwards, the cultures were prepared as a few tubes with 4-6 times of 10x dilution, and culture for an overnight growth in order to reach OD_{600} between 0.1 and 0.4 for the next day's imaging experiment. To perform acute glucose starvation, 96-well (Cellvis, Cat. no. P96-1.5H-Nor) or 384-well (Cellvis, Cat. no. P384-1.5H-Nor) glass bottom imaging plates were precoated with 1 mg/mL concanavalin A (Alfa Aesar, Cat. no. J61221) before applying the yeast cell culture. 10 min later when cells settled down to the bottom of the imaging plate, the culture medium was removed completely, and four additional wash of cells with SCD medium, and then perform imaging recorded as the initial 0 min time point. Afterwards, SCD medium was removed, followed by four additional wash of the cell with treatment medium. Cells were then imaged at the correspondent time points afterwards.

To perform acute glucose starvation, SC medium supplemented with 2% sorbitol (to balance the osmotic pressure exerted by 2% glucose) was used. To perform amino acids starvation, SC medium supplemented with 2% glucose but without any amino acids was used. To induce oxidative stress, cells were treated with SC medium with 2% glucose and 0.3 mM H_2O_2. To perform ATP depletion experiment, SC medium supplemented with 80 mM sorbitol, pH adjusted as 5.5, 2-Deoxy-d-glucose and antimycin A were used in combination at 20 mM and 10 μM, respectively.

To perform hypotonic shock in yeast cells, yeast cells were diluted at low density (around OD = 0.0015) and cultured in synthetic complete with 500 mM KCl (SCD+500 mM KCl) for overnight to reach log phase growth the other day morning (OD < 0.5). And cells were attached on a 96-well glass bottom plate with 1 mg/mL concanavalin A before switching to acute glucose starvation medium (SC medium supplemented with 2% sorbitol).

Drug treatments

Cycloheximide was used at a final concentration of 100 μg/mL in all yeast experiments, while for mammalian cell experiments, 20 μg/mL of cycloheximide was used as a final concentration. Puromycin and des-methyl, des-amino pateamine A (DMDA PatA, a gift from Daniel Romo lab) were used at a final concentration of 100 μg/mL and 10 nM, respectively, in all mammalian cell culture experiments. ISRIB was used at a final concentration of 200 nM in all mammalian cell culture experiments. Sodium arsenite was used at either 250 μM (Figures 5H and 5I) or 100 μM (Figure 5A) in mammalian cell culture experiments.

Sucrose gradient to fractionate polysomes

60 mL yeast cell culture in SCD medium reaching OD_{600} around 0.4 were collected by 3000 g centrifugation. And cells were washed with treatment medium before switching to the correspondent medium for additional 30 min culture, and 100 μg/mL cycloheximide was added to the culture before collected again by centrifugation and freshly frozen in a −80°C freezer. To prepare sucrose gradient, four layers of sucrose solutions (2.7 mL each) were prepared in concentrations as 10%, 23.3%, 36.6%, and 50%, where the sucrose were layered from bottom to top as high to low concentrations in 14x89 mm ultracentrifuge tubes (Beckman, 14x89 mm polypropylene centrifuge tubes, Cat. no. 331372), and each layer of sucrose was freshly frozen at −80°C for 20 min before adding a second layer on top. To prepare cell lysis, polysome buffer (10 mM Tris, 10 mM $MgCl_2$, 100 mM KCl, 6 mM β-mercaptoethanol, 100 μg/mL cycloheximide, protease inhibitors (Thermo Scientific, Cat. no. A32961) pH 7.5) were freshly prepared, and cell pellets were washed and then resuspended in 500 μL polysome buffer in the glass tube (Fisher Scientific, Cat. No.14-961-32). Afterwards, 0.5 mm glass beads (BioSpec Products, Cat. No.11079105) were added as half of the volume in cell suspension and vortexed four times as 30 s each, with 1 min rest time on ice in between. And then all the cell lysis extract were transferred to a new 1.5 mL tube, and 300 μL polysome buffer were used to wash the glass beads then combined with the cell lysis extract. To clarify the cell lysis extract, 10 min of centrifugation at 15000 g was performed at 4°C. And the supernatant of cell lysis extract was transferred to a new 1.5 mL tube, where the OD_{260} was measured by spectrophotometer. 9 units of OD_{260} cell lysis extract of each sample was then layered on top of the sucrose gradient, all the samples were then centrifuged at 39,000 rpm (Beckman, SW 41 Ti Swinging-Bucket Rotor) at 4°C for 2.5 h. Afterwards, the samples were subjected to the fractionation system for analysis (Brandel, SYN-202 density gradient fractionation system).

Passive rheological probes imaging and single particle tracking

To image 40nm-GEMs in *Saccharomyces cerevisiae*, TIRF Nikon TI Eclipse microscope in highly inclined thin illumination mode (HILO) was used at GFP laser (49002-ET-EGFP)excitation with 100% power. Fluorescence was recorded with a scMOS camera (Zyla, Andor) with a 100x Phase, Nikon, oil NA = 1.4 objective lens (part number = MRD31901, pixel size: 0.093 μm). Cells were imaged at 100 Hz (10 ms per frame) for a total of 4 s. To image uNS particles in *Saccharomyces cerevisiae*, Andor Yokogawa CSU-X confocal spinning disc on a Nikon Ti2 X1 microscope was used at 488 nm excitation with 10% power. Fluorescence was recorded with a sCMOS Prime 95B camera (Photometrics) with a 60x objective (pixel size: 0.18 μm), at a 100 ms image capture rate, with a time step for 30 s. To image 40nm-GEMs in U2OS mammalian cell lines, Andor Yokogawa CSU-X confocal spinning disc on a Nikon Ti2 X1 microscope was used at 488 nm excitation with 100% power. Fluorescence was recorded with a sCMOS Prime 95B camera (Photometrics) with a 60x objective (pixel size: 0.18 μm), at a 10 ms image capture rate for a total of 2 s.

The tracking of particles was performed with the Mosaic suite of FIJI,[130] using the following parameters. For yeast 40nm-GEMs: radius = 3, cutoff = 0, Per/Abs: variable, a link range of 1, and a maximum displacement of 7 px, assuming Brownian dynamics. For yeast μNS particles: radius = 3, cutoff = 0, Per/Abs: variable, a link range of 1, and a maximum displacement of 5 px, assuming Brownian dynamics. For mammalian cell 40nm-GEMs: radius = 2, cutoff = 0, Per/Abs: variable, a link range of 1, and a maximum displacement of 5 px, assuming Brownian dynamics.

All trajectories were then analyzed with the GEMspa (GEM single particle analysis) software package that we are developing in house: https://github.com/liamholtlab/GEMspa/releases/tag/v0.11-beta. Mean-square displacement (MSD) was calculated for every 2D trajectory, and trajectories continuously followed for more than 10 time points were used to fit with linear time dependence based on the first 10 time intervals to quantify time-averaged MSD: $MSD(T) = 4D_{eff}T$, where T is the imaging time interval and D_{eff} is the effective diffusivity with the unit of $\mu m^2/s$. To determine the ensemble-time-averaged mean-square displacement (MSD), all trajectories were fitted with $MSD(\tau)_{T-ens}=4D\tau^{\alpha}$ where α is the anomalous exponent, with $\alpha = 1$ being Brownian motion, $\alpha < 1$ suggests sub-diffusive motion and $\alpha > 1$ as super-diffusive motion. To generate region of interest (ROI) for marking individual yeast cell, cellpose python package (https://github.com/mouseland/cellpose) was used to segment based on the bright field images or the average projection intensity of 40nm-GEMs or μNS particles. These ROI were then input into GEMspa to quantify single cell effective diffusion, with at least three trajectories averaged for individual yeast cells. We used the median value of D_{eff} for single cell data to represent each condition.

For mammalian cell quantification of D_{eff}, the same field of the view of the cytosolic region covering the whole cell from individual cell was cropped before and after drug treatment, and the median value of D_{eff} from all trajectories within the cropped region were quantified, and D_{eff} from the same cell after drug treatment was normalized to before drug treatment D_{eff} as a fold change value. Or all analyzed trajectories within one cell were averaged to present single cell D_{eff} for each condition.

Step sizes for all trajectories were extracted from GEM-Spa, to reflect the distance (with the unit of μm) of particles traveled for a given time interval: 100 ms for 40nm-GEMs and different time intervals for μNS particles. To measure the average intensity of μNS particles from GEM-Spa, a fixed radius (radius=3) was used along the movie series, and the mean intensities of particles were measured at all the tracked frames and then summarized as average mean intensity.

Normalized velocity autocorrelation was analyzed using a custom-developed MATLAB (R2019a) program based on trajectories extracted from either experimental data or simulations.[44] Initially, velocities within specific time intervals were calculated for each trajectory, resulting in velocity time series along either the x or y directions. Subsequently, autocorrelation functions were applied to these velocity time series, generating outputs as a function of various time delays. Due to the orthogonality, the autocorrelation functions from both x and y direction were summed and were then normalized by the values at the zero time delay. For each condition, the normalized velocity autocorrelation functions were averaged across all trajectories.

Live yeast cell ATP sensor and pH sensor imaging and quantification

To image the ratiometric ATP sensor QUEEN in *Saccharomyces cerevisiae*, TIRF Nikon TI Eclipse microscope was used with 100x Phase, Nikon, oil NA = 1.4 objective lens (part number = MRD31901) at around 25°C. Both sensors were illuminated with LED light sources at a single z-plane using DAPI filter set (value recorded as 410ex): excitation filter (Excitation wavelength/ Bandwidth (FWHM) = 401/17 nm) and an emission filter (Emission wavelength/ Bandwidth (FWHM) = 444/58 nm), GFP filter set (value recorded as 480ex): excitation filter (Excitation wavelength/ Bandwidth (FWHM) = 470/40 nm) and an emission filter (Emission wavelength/ Bandwidth (FWHM) = 525/50 nm). The quantification of QUEEN sensor ratio is mainly followed by standard protocol.[131] Basically, individual yeast cells were segmented with 200x200 pixels ROI and the average intensity was measured after background subtraction. And the QUEEN sensor ratio was calculated as 410ex/480ex, where a reducing ratio indicates a decrease of intracellular ATP level.

To generate a calibration curve with pH sensor pHurion integrated into the yeast cells (LH4820), we used the McIlvaine buffer to prepare extracellular medium with buffer pH ranging from 5-8, mainly by varying the amount of 0.2M disodium phosphate and 0.1 M citric acid. Yeast cells were permeabilized by 100 μg/mL digitonin (Sigma-Aldrich Cat. no. D141-100MG). The pH sensor pHurion was imaged using the same fluorescence channels as the ATP sensor QUEEN; the sensor ratio was calculated as 410ex/480ex for each measured pH. A linear model was fitted to determine the standard curve, so that the intracellular pH can be quantified upon acute glucose starvation.

Live yeast cell RNP granules and Q-bodies imaging and quantification

Yeast cells expressing P-bodies protein marker (Dcp2-mScarlet), SGs protein marker (Pab1-mNeoGreen) or Q-bodies protein marker (Hsp42-mScarlet) were immobilized on the 1 mg/mL concanavalin A precoated 384-well or 96-well glass bottom imaging plate. And yeast cells were imaged on TIRF Nikon TI Eclipse microscope with 100x Phase, Nikon, oil NA = 1.4 objective lens (part number = MRD31901) at around 25°C, LED light were used to illuminate the preselected field of views, and fluorescence intensity were recorded using GFP and RFP filter set. Acute glucose starvation mediums with/without cycloheximide were switched before imaging. And time lapse movies were set up to record every 10 min for a total of 120 min. 6-μm Z-stacks of yeast cells were taken with 0.5-μm steps between frames. The Z-stacks were projected using average intensity in Fiji, trackmate were used to identify P-body condensates or Q-bodies in individual cells, and number of P-bodies or Q-bodies were tracked along the time series.

Live yeast cell total cell volume, vacuole volume and cytosolic volume measurement

Yeast strain (LH4406) was cultured to log phase and immobilized on concanavalin A precoated 96-well glass bottom imaging plate for 10 min. The remaining cell culture was removed and cells were either washed by synthetic complete medium or acute glucose starvation medium for three times in the imaging chamber, and cells were kept in the respective medium for additional 30 min before imaging. 6-μm Z-stacks of yeast cells were taken with 0.2-μm steps between frames on Nikon TI Eclipse spinning disc confocal microscope. In order to quantify the total cell volume or vacuole volume, the Z-stack images were visually scanned in ImageJ to determine and record center point coordinates for each individual cell or vacuole, based on the respective plasma membrane marker (NeoGreen-PLCΔ-PH2) and vacuole membrane marker (Vph1-TdTomato). And the adopted Matlab script was used to identify and segment individual cells and vacuoles through the z-slice, reconstituting them as ellipses for volume quantification.[132] The cytosolic volume was calculated by subtracting the vacuole volume from total cell volume in individual yeast cells.

Immunofluorescence

U2OS cells were seeded in the 24-well glass bottom plate (Cellvis, Cat. no. P24-1.5H-Nor) to reach around 60%–70% confluency the next day. After 30 min treatment with the indicated protein translation inhibitors, cells were immediately fixed with flesh 4% paraformaldehyde (Electron Microscopy Sciences, Cat. No. 15714) for 10 min at room temperature. The cells were subsequently washed three times with 1x PBS, and permeabilized with 0.2% Triton X-100 (Fisher Scientific, Cat. No. 9002-93-1) in 1x PBS for 15 min at room temperature. And then cells were blocked with 1% BSA, in PBST (PBS+ 0.1% Tween 20) for 1 h before applying the primary antibodies (1:250 dilution was applied for anti-G3BP1 antibodies) for overnight incubation at 4°C. The next day, solutions were removed and the cells were washed four times with 1x PBS, and incubated with secondary antibodies (1:1000 dilution was applied for anti-Mouse IgG (H+L)) in 1% BSA, in PBST at room temperature for 1 h in the dark. Afterwards, solutions were removed and cells were washed with 1x PBS for four times before staining with 1 μM Hoechst 33342 (Thermo Fisher Scientific 62249) for 15 min at room temperature in the dark and were subsequently stored in 1x PBS at 4°C in the dark until imaging. The fixed plates of cells were imaged on an Andor Yokogawa CSU-X confocal spinning disc on a Nikon TI Eclipse microscope at room temperature. The fluorescence signals were obtained using DAPI epifluorescence (excitation wavelength/bandwidth: 395/25 and emission wavelength/bandwidth: 460/50), RFP laser (Coherent, filter: ET605/70m) and far red (Coherent, ET700/75m) lasers, and images were captured using a Prime 95B scMOS camera (Photometrics) with a 60x/1.49 numerical aperture objective lens. 8-μm Z-stacks of G3BP1 and Dcp1 fluorescence were taken with 0.5-μm steps between frames. The Z-stacks were projected using maximum intensity in Fiji and P-bodies numbers (Dcp1 foci) were manually counted in each cell.

Poly-dT FISH Imaging

U2OS cells were seeded in the 24-well glass bottom plate (Cellvis, Cat. no. P24-1.5H-Nor) to reach around 60-70% confluency the next day. After 30 min treatment with 10 nM DMDA PatA, cells were immediately fixed with flesh 4% paraformaldehyde for 10 min at room temperature. The cells were subsequently washed three times with 1x PBS, and permeabilized with 0.2% Triton X-100 in 1x PBS in room temperature for 15 min. And then cells were washed two times with 1x PBS and one time with 2x SSC (300 mM Sodium chloride, 30 mM Sodium citrate pH8). Pre-hybridize the cells with the 200 μL pre-warmed (37°C) hybridization buffer (Molecular instruments, HCR hybridization buffer) in a 37°C humidified chamber for 30 min. 25 ng of poly-dT-alexa647 probe was prepared for each sample in the HCR hybridization buffer, and applied it to each well. And the plate was kept in a 37°C humidified chamber in the dark overnight. The next day, the hybridization buffer was removed and cells were washed twice vigorously with a pre-warmed HCR washing buffer (Molecular instruments), followed by an additional 2 times wash of 1x PBS. 1 μM Hoechst 33342 was applied into each well and incubated in dark for 15 min in 1x PBS to stain the nucleus. Cells were subsequently stored in 1x PBS at 4°C in the dark until imaging. The fixed plates of cells were imaged on an Andor Yokogawa CSU-X confocal spinning disc on a Nikon TI2 X1 microscope at room temperature. The fluorescence signals were obtained with DAPI (Coherent, filter: ET455/50m) and far red (Coherent, ET700/75m) lasers, and images were captured using a Prime 95B scMOS camera (Photometrics) with a 60x/1.49 numerical aperture objective lens. 10-μm Z-stacks of poly-dT FISH fluorescence were taken with 0.2-μm steps between frames.

Blue-light activation of optogenetic artificial RNP condensates

Two days post transient transfection of pLH1972 or pLH2126 into U2OS 40nm-GEMs cells in the 6-well glass bottom plate, both CRY2-mCherry and CRY2-PUM.HD-mCherry proteins were expressed as diffusive pattern in the cytoplasm. On the day of the experiment, cells were mounted on a Nikon TI2 X1 spinning disk confocal scanning microscope, equipped with a 60x/1.49 numerical aperture objective lens and incubator to maintain 37°C and 5% CO2. Individual cells with CRY2-mCherry/CRY2-PUM.HD-mCherry expression were pre-selected initially, and 40nm-GEMs movies were recorded as previously described in the STAR Methods section, which reflects particle diffusivity before light induced artificial pumilio granule formation. To apply blue light to induce artificial pumilio granule formation, GFP laser (Coherent, filter: ET525/36m) with 25% power were illuminated to the field of view every 5 s for 5 min, and artificial RNP condensates signal were recorded by RFP laser (Coherent, filter: ET605/70m). Afterwards, 40nm-GEM movies were recorded again.

Cryo-electron tomography

Saccharomyces cerevisiae (BY4741) were recovered from frozen stocks (stored at −80°C) and streaked onto YPAD agar plates. Cells were grown for 3 days at 30°C before single colonies were re-streaked onto fresh plates and grown for 2 days as described above. Single colonies were picked from these plates to inoculate 20 mL of synthetic media supplemented with 20 mM dextrose (glucose control medium). The liquid cultures were incubated overnight at 30°C and shaking at 165 rpm (NCU-Shaker mini, Benchmark) to grow cells to the exponential growth phase. Cells at an OD_{600} of 0.5–0.6 were centrifuged for 3 min at 3000 rpm, resuspended in either 1 mL of glucose control medium or synthetic medium supplemented with 100 mM sorbitol (starvation medium) and washed twice. Each washing step consisted of centrifugation at 4,000 rpm for 3 min (Eppendorf 5424R centrifuge), discarding the supernatant and replacing it with 1 mL of the respective medium. Cells were incubated either in glucose control medium or starvation medium shaking at 165 rpm for 30 min before plunge-freezing.

Plunge-freezing was performed using a Leica EM GP2 (Leica Microsystems), set to 22°C and 99% humidity. 4 μL of the cell suspension were deposited on glow discharged holey Quantifoil silicon dioxide grids (R1/2, Cu 200 mesh grid, Quantifoil Micro Tools), and grids were blotted from the reverse side for 1–2 s before being plunged into liquid ethane cooled to the temperature of liquid nitrogen. For the subsequent steps of cryo-focused ion beam (cryo-FIB) milling and cryo-electron tomography (cryo-ET), grids were kept at liquid nitrogen temperature.

Cellular slices (lamellae) with a thickness of approximately 200 nm were generated by cryo-FIB milling.[133–135] Grids with vitrified cells were mounted into custom-made AutoGrid cartridges and transferred into an Aquilos cryo-focused ion beam/scanning electron microscope (FIB/SEM dual-beam microscope, Thermo Fisher Scientific) using a 45 degree pre-tilt shuttle. Grids were initially sputter-coated with platinum and coated with organometallic platinum using the gas injection system to render the samples conductive and to reduce curtaining artifacts that can occur during FIB milling. Next, positions for lamella generation were determined and refined for eucentricity using MAPS3 (Thermo Fisher Scientific). Milling was performed with a gallium ion beam at 30 kV at a stage tilt angle of 20 degrees. The SEM was used to monitor progress during the milling process (10 kV, 50 pA). Automated rough-milling was conducted in a stepwise fashion with SerialFIB[128] using currents of 1 nA, 0.5 nA and 0.3 nA to thin down the cells to 5 μm, 3 μm and 1 μm, respectively. Finally, lamellae were manually thinned to the target thickness of 200 nm using a current of 50 pA. To render the lamellae conductive for subsequent cryo-ET, a final platinum sputter coating was applied for 3–5 s (1 kV, 10 mA, 10 Pa).

Cryo-electron tomograms were acquired on a Titan Krios microscope operated at 300 kV (Thermo Fisher Scientific) equipped with a field-emission gun, a quantum post-column energy filter (Gatan) and a K3 direct detector (Gatan). Data was collected in low-dose mode using automation scripts in SerialEM.[121] Tilt series were acquired from -60 ° to +60 ° in 2 ° increments at a magnification of 26,000x with a calibrated pixel size of 3.425 Å, using a dose-symmetric tilt scheme,[136] defocus range of 2-4 μm, and keeping the total accumulated dose below 150 e^{-}/A^{2}. 14 tilt series were acquired for the glucose control and 26 tilt series for the starvation condition. Prior to tomogram reconstruction, tilt movie frames were corrected for gain reference and beam-induced motion in Warp 1.0.9[123] alongside contrast transfer function (CTF) estimation. Tomograms were aligned and reconstructed by weighted back-projection in AreTomo[137] at 4x binning, corresponding to a pixel size of 13.7 Å.

For localization of ribosomes, 4 tomograms from the glucose control and 10 from the glucose starvation condition were selected for further analysis based on high data quality (sufficient signal-to-noise ratio due to optimal specimen thickness). Initial particle picking was carried out with DeePiCt[59] on the 4x binned data. To facilitate particle localization and for visualization, tomograms were preprocessed via amplitude spectrum matching to a tomogram of high contrast, implemented in DeePiCt.[59] The 3D CNN for ribosome detection (depth *D*=2, initial features *IF*=4) was trained on 29 ground truth tomograms (9 volta phase plate, and 20 defocus only *S. pombe* and *S. cerevisiae* tomograms) annotated for ribosomes through a combination of template matching, CNN-based predictions using a pretrained network (de Teresa-Trueba et al.[59]; full_vpp_ribo_model_IF4_D2_BN.pth accessible from https://github.com/ZauggGroup/DeePiCt), and completed by manual annotation. Performance evaluation of the network resulted in an area under the precision-recall curve (AUPRC) with a median of 0.46 in the *S. cerevisiae* defocus glucose control data., The 3D CNN thus detected only around 50% of the ribosomes in the data. Undetected particles were therefore picked manually using e2spt_boxer.py in EMAN2[127] to complete the ribosome annotations in the data to an estimated 90%–95% coverage. The complete particle coordinates were then used to reconstruct unbinned or 2x binned subtomograms and corresponding CTF models in Warp 1.0.9[123] at box sizes of 192 x 192 x 192 voxel or 96 x 96 x 96 voxel, respectively, and a particle diameter of 350 Å. Subtomograms of 22,459 particles from the glucose control and 51,846 particles from the glucose starved cells were reconstructed from the respective tomograms. 3D alignment and classification of the subtomograms was carried out in RELION 4.0.1[125] using a published *S. cerevisiae* ribosome map (EMDB 3228,[117] scaled and low-pass filtered to 60 Å) as a reference. Multiple rounds of 3D refinement were run in RELION. For the starvation condition, the multi-particle refinement was further carried out in M.[124] The resolution of the averages was calculated based on Fourier Shell Correlation (FSC, cut-off criterion 0.143) between the two independently refined half maps. The resolution estimate was 17.8 Å/px for the 2x binned (6.85 Å/px) average from glucose control tomograms and 10.2 Å/px for the unbinned (3.425 Å/px) average from the starved cells. Averages were visualized in ChimeraX 1.1.1.[126]

Based on the ribosome subtomogram averages, the positions of the mRNA entry and exit sites were determined on the maps, and the refined poses for the individual ribosomes used to calculate the distances between the exit site of each ribosome to the entry site of its neighboring ribosome with a custom script in MATLAB 2019a.[58] The distance distribution from a ribosomes exit site to the nearest entry site of another ribosome was plotted as a histogram. Gaussians with different cutoff values were fitted to the polysome peak of this distribution, and a distance threshold of 8 nm was found to best describe the data. Consequently, ribosomes within the range of 8 nm of each other were assigned to the same polysome. Finally, each polysome was labeled with a unique identifier and the ribosomes making up the polysome were given sequential numbers. Based on this data, the fraction of ribosomes in polysomes was calculated from the total ribosome counts and the remaining ribosomes were assigned to a monosome fraction. Further, the percentage of ribosomes engaged in different length polysomes was determined by calculating the number of ribosomes assigned to each polysome and determining the frequency of each polysome length. To compare the starvation-induced reduction in polysome fractions determined based on the sucrose gradient fractionation and on the cryo-ET data, polysome fractions were normalized to the respective glucose control fractions. To derive polysome fractions at different distance cutoffs, we repeated the above analysis for mRNA exit to entry site distances ranging from 8 to 25 nm.

Coarse-grained molecular dynamic (MD) simulation

We developed a simplified coarse-grained MD simulation framework to represent the most crucial elements of the experimental conditions. Our simulations consist of a mix of spherical particles of diameter 30 nm to represent ribosomes, and varying diameters ranging from 25 to 125 nm representing mesoscale particles. Polysomes can be formed by taking groups of 6 ribosomes in the initial configuration and linking them with harmonic springs of length 40 nm and a spring constant of 20 k_BT/nm^2. In the simulations presented here, each ribosome in a polysome is linked by a 20 nm spring to a virtual particle of 20 nm diameter halfway between ribosomes. This virtual particle only interacts with other virtual particles using a Weeks-Chandler-Anderson (WCA) potential (described below), and serves to prevent polysome chains from crossing, but does not change the excluded volumes for GEMs.

The fraction of ribosomes that are polymerized is varied as a simulation parameter from 0 to 1. A simulation box of size 860 nm per side with periodic boundary conditions was used. The number of ribosomes in the box was set to the integer number that was closest to the target volume fraction of ribosomes. The number of GEM particles was set to the integer number which was closest to 0.5% volume fraction, but was set to 1 for the largest GEMs even if this exceeded 0.5%. RNA and GEM particles and virtual polysome linker particles had a strictly repulsive interaction of a WCA form,[138]

$$V_{WCA}(r_{ij}) = 4\epsilon\left((\sigma_{ij}/r_{ij})^{12} - (\sigma_{ij}/r_{ij})^{6}\right) + \epsilon, r_{ij} < 2^{(1/6)}\sigma_{ij}, otherwise\ 0$$

With $\boldsymbol{\sigma_{ij}}$ being the average of the diameters of the pair of particles being considered, and $\epsilon = 5\,k_BT$.

Additionally, 40 nm spheres representing free RNA were put in the box at concentrations ranging from 0 to 5 micromolar. These particles interact with each-other and with ribosomes through a Lennard-Jones attractive potential[139] with $\boldsymbol{\sigma_{ij}}$ set using the same mixing rule, and the potential shifted and cut off at 2.5 $\boldsymbol{\sigma_{ij}}$. ϵ_{LJ} =1.0 between RNA and ribosomes, and between RNA and RNA, but ϵ_{LJ} =0 between RNA and GEMs.

$$V_{LJ}(r_{ij}) = 4\epsilon\left((\sigma_{ij}/r_{ij})^{12} - (\sigma_{ij}/r_{ij})^{6}\right) + shift, r_{ij} < 2.5\,\sigma_{ij}, otherwise\ 0$$

MD simulations were performed using the software HOOMD-Blue[120] version 3.7.0. Particle positions are evolved using Brownian dynamics (BD) at a temperature of k_BT=1 with a friction coefficient of 0.01, and a time step of 0.0001 simulation units. Simulations were initialized with particles randomly positioned in a box of size 5000 nm per side. Minimization was performed in up to 5 stages of 5000 steps using the FIRE minimization algorithm with a timestep of 0.001, with a force tolerance of 1×10^{-4} and energy tolerance of 1×10^{-7}. Particle velocities were then initialized from a Boltzmann distribution at temperature k_BT=1. BD was performed for 10^5 steps to relax the system, and then the box was compressed to the target volume over 10^5 steps while simultaneously performing BD. Finally, a production run BD of 5×10^6 steps was performed and analyzed, saving every 10000 steps, corresponding to one time unit. Most probable displacements were computed by taking the location of the peak in a histogram of root-mean-squared displacements for all GEM particles computed every 100 snapshots. Videos and images of MD simulations were rendered using OVITO.[140] Rendered videos were of 10x longer simulations to aid visualization.

QUANTIFICATION AND STATISTICAL ANALYSIS

Images were quantitated with FIJI and MATLAB. Single particle tracking data was analyzed with GEMspa.[141] Graphs were generated by GraphPad Prism 10 (GraphPad Software). Statistical analysis was performed with GraphPad Prism 10 (GraphPad Software). Further statistical details can be found in the figure legends and STAR Methods.